Image Guided Navigation for Minimally Invasive Surgery

Hua Zhong

October 23, 2007

Computer Science Department
Carnegie Mellon University
Pittsburgh, Pennsylvania 15213

Abstract

In this thesis, we present a catheter navigation system for minimally invasive surgery. The core of such a navigation system is to register pre-operative high resolution 3D or 4D heart model with intra-operative heart shape model to build a combined heart shape. With such a combine shape model the intra-operative catheter motion can be tracked and displayed with it. Then clinicians can easily navigate catheters inside human heart. The most difficult part of such a registration is how to quickly and reliably capture intra-cardiac heart shape measurement. We designed a 3D ultrasound catheter "virtual touch" technique which can capture heart shape measurement during operation in a much faster and more accurate way than conventional manual collection method. Our system can use 4D model and points which captures the heart shape change during one cardiac cycle for registration. To address non-rigid shape changes from breathing cycles and other sources, our system has a local non-rigid registration component to further correct the high resolution pre-operative shape model based on intra-operative realtime shape measurement from "virtual touch".

Contents

1 Introduction

This thesis is for an image guided catheter navigation system for minimally invasive interventions inside human heart. The system can automatically register the intra-operative heart shape information with a pre-operative heart shape model from CT scan. Then it can render the locations of catheters relative to the heart shape model in real time to help clinicians to navigate the catheters. We focus on an navigation system for left atrium ablation procedure in this proposal. But the system is also useful for general navigation of medical instruments inside human body.

1.1 Minimally Invasive Heart Surgery

Traditionally, in a heart surgery, doctors need to open the chest of patient to operate on his/her heart. This kind of surgery involves tremendous pain and takes a long time for patients to recover. Recent years, it is more and more popular to use minimally invasive surgery methods to do heart surgery. With minimally invasive methods, there is no need to open patient's chest. Instead, a thin and flexible plastic tube is inserted into patient's heart through veins. This plastic tube is called a catheter. At the tip of the catheter, various devices can be installed for different interventions or to guide surgery. For example, an ablation device can be fit at the tip of a catheter to do left atrium ablation procedure, an retractable needle can be used to inject medicines, or an ultrasound catheter can be used to inspect heart from inside.

Our system described in this thesis is originally designed for Left atrium ablation procedure which is to cure atrial fibrillation. During the surgery, an ablation catheter is inserted into the left atrium through veins. Clinicians need to navigate the ablation catheter to ablate the areas where left and right pulmonary veins meet the left atrium.

Minimally invasive surgery has so many advantages. It also has limitations. For example without opening patient's chest it is impossible to directly visualize the position of catheters inside the heart. So far clinicians usually use fluoroscopy (X-ray) imaging device to see where the catheter is inside a heart. But problems are

1. Fluoroscopy imaging device can not be running for long time because of radiation. It can only provide a few snapshots and then has to be turned off.
2. Heart wall in fluoroscopy images is not clearly visible to human eyes. Usually it is just a blurred shadow and hardly to precisely see the exact boundary.
3. Each fluoroscopy image is only a 2D image. Multiple images have to be manually registered in clinicians mind to guess the 3D topology.

1.2 Current Navigation Systems

Navigation of catheter inside heart usually involves registering intra-operative data with a high resolution pre-operative heart model. After registration, intra-operative real time position data can be displayed with pre-operative shape models to enable intuitive navigation. The accuracy and speed of the registration determines the efficiency of the whole navigation system.

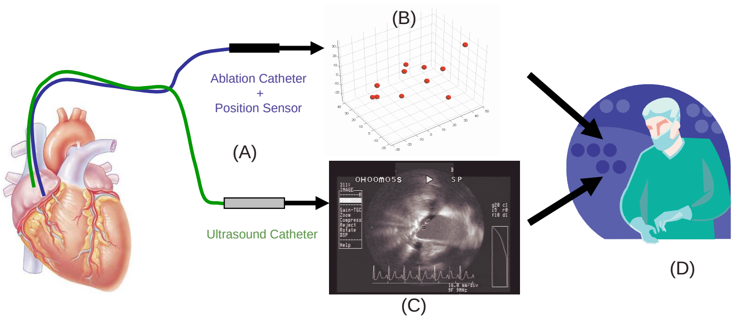

Figure 1: Current left atrium ablation procedure: (A) An ablation catheter with position sensor and an ultrasound catheter are inserted into the heart. (B) Clinicians can see the 3D position of ablation catheter in one monitor and (C) the ultrasound image in another monitor. (D) They have to couple the data together in their mind to figure out the actual location of the ablation catheter inside the heart. Only highly experienced clinicians can do it efficiently.

There are systems available for registering solid bone images with position sensors such as HipNav [11]. HipNav requires clinicians to touch the bone's surface with position sensor at several locations, and then register these 3D locations with 3D bone model from CT or MRI. 3D registration works well with solid objects like bones. For cases such as left atrium, because it is beating during the procedure, the shape of left atrium will change periodically. Thus the registration problem becomes more complicated than bones.

Recent years, some registration and navigation systems for left atrium ablation procedure have been developed [25] as well as commercially available Carto Merge system. As seen in Figure 2 left column, these systems register the 3D heart model from pre-operative CT scan with the intra-operative heart surface points captured by manually moving ablation catheter with magnetic position sensor to touch the inner heart wall. This registration will align the 3D heart model with the magnetic tracking system using ICP [1] algorithm. After the registration, the system can visualize the heart model and the catheter tip together. Also [17] incorporates 3D MRI image with EAM points for registration and navigation and suggest aorta points can help the 3D registration. [9] evaluated the accuracy of such 3D registration between EAM points and CT model with a dog's heart.

The problem with such system is that first they use only a rigid 3D model with ICP [1] algorithm for registration. As we know, the heart is beating and breath cycles can change the heart shape as well. The protocol of Carto Merge suggest clinicians to capture surface points at 0% of a cardiac cycle and at the end of expiration. Since the breath cycle and cardiac cycle are independent of each other, it is very difficult to capture a point at both end of expiration and 0% of a cardiac cycle. So the accuracy of the registration can not be guaranteed. Second, to capture each surface point, clinicians need to manually move the ablation catheter to touch the heart wall. The touch is verified by fluoroscopy images. As we have stated before about the shortcom-

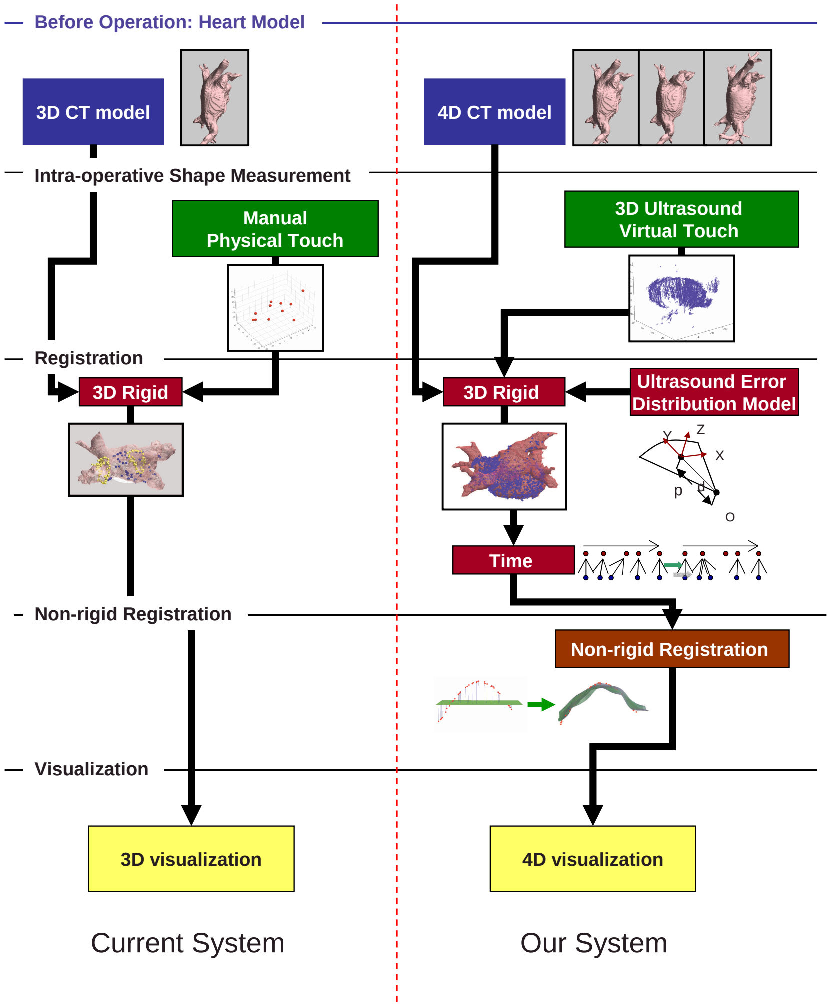

Figure 2: Comparison of current available commercial system and our proposed system.

ings of fluoroscopy imaging device, it will eventually affects the quality of registration points. Now some clinicians are using intra-cardiac ultrasound catheters to guide ablation catheters and verify the touch of ablation catheter to the heart wall [22] [26]. In this case, an ultrasound catheter is inserted into the left atrium. From the real time ultrasound images captured by the ultrasound catheter, clinicians can clearly see the ablation catheter touching the heart wall. The verification of touching is much better than with fluoroscopy images. This is the best scenario currently clinicians can have. But it doesn't improve the speed. To capture 50-60 registration points, an experienced clinician may need approximately 10-25 minutes. Moreover in order to capture points which are well spread on the heart wall to ensure higher registration accuracy, more points are needed.

1.3 Our Approaches

1.3.1 Combining Pre-operative and Intra-operative heart Models

Our approach for navigation inside heart is to combine high quality pre-operative heart model from CT scan or MRI with realtime intra-operative heart shape measurement from our new ultrasound "virtual touch" technique. Pre-operative heart model is of high resolution while the shape may not be exactly the same as the heart during operation. Intra-operative heart model generated by our ultrasound "virtual touch" is exactly what the heart looks like during operation. But due to limited flexibility of catheters and size constraints of the heart chambers, it may not cover everywhere of the heart. By combining these two models together using registration, we can provide doctors a high-resolution realtime heart model which has the same shape as the real heart during the operation. This combined model then has the advantage of both pre-operative and intra-operative heart models while not their shortcomings. Then the navigation will be based on this combined model.

To combine the two models, we need to do several registrations. We assume the two heart models should be the same shape unless some small local shape differences. Then first we need to do the global shape registration which will put the two models into a single coordinate systems. Usually this will be the coordinate system of our magnetic position sensor system during the operation so that later the motion of catheters can be easily displayed with the heart model. With a beating heart, if both models are captured as a 4D space-time model, we also need to do time registration. Eventually, to correct non-homogeneous small local shape changes caused by different breath phases, we have a non-rigid local registration component to seamlessly wield the two models into one high-resolution realtime heart model.

After the registration, navigation can be easily done with various way of visualizing the position of catheters inside the heart. What doctors will see on the monitor is the combined model representing the current heart shape and a realtime catheter model representing the current catheter location inside the heart.

1.3.2 Comparison to Current Commercial Systems

The overview diagram of our system is shown in Figure 3. Comparing to the commercial system like shown in Figure 2, our system replaced each component of the system with better ones and added non-rigid registration component.

For building the intra-cardiac heart model, instead of touching the heart wall manually with a catheter tip, we use a new catheter which combines ultrasound sensor, magnetic position sensor and ablation unit together and encapsulates them in one catheter. This catheter can capture tens of thousand of high quality surface points within a few minutes without physically touch the heart wall. We call this technique "Virtual Touch". "Virtual touch" can be used to scan heart walls to generate an intro-operative 3D or 4D heart shape model which represent the current shape of the heart during operation. It works like a laser 3D scanner only with ultrasound.

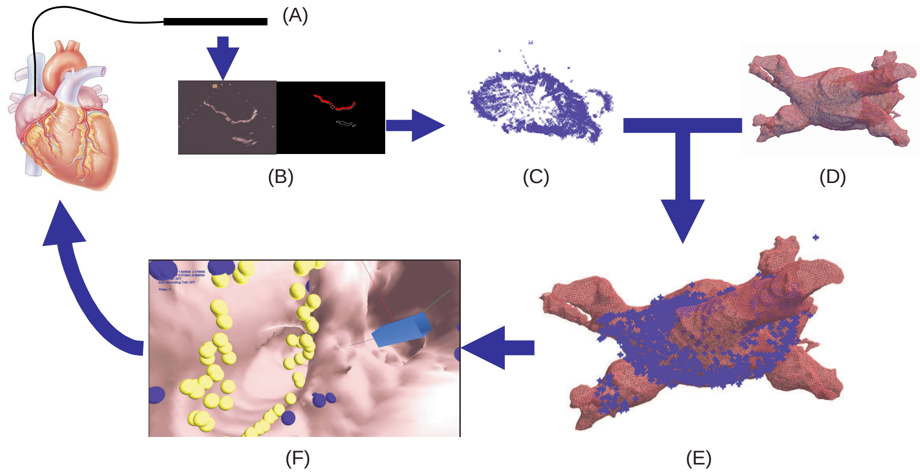

Figure 3: System Diagram: (A) A catheter which combines ablation, ultrasound and position sensor (6 DOF). Clinicians use this catheter to scan the heart wall before registration. (B) Our system detect heart wall pixels in the ultrasound images. (C) With the position sensor's read-out and ECG signals, 4D coordinates of the wall pixels are automatically reconstructed. (D) 4D heart model reconstructed from pre-operative CT scan. (E) Using 4D + local non-rigid registration, our system registers the points to the model. (F) Real-time visualization of catheter position inside heart then is available for clinicians to guide the ablation procedure.

Unlike laser, ultrasound beams have a finite width of 3-6mm for common intracardiac ultrasound catheters. This beam width makes the ultrasound image plane not a infinitely thin plane but a plane with 3-6mm thickness. Any 3D ultrasound reconstruction algorithm ignoring such image plane thickness will introduce errors. Especially this error is dependent on the intersecting angle of ultrasound image plane and the object surface it scans. We provide an easy and reliable way to correct errors caused by finite image plane thickness and it can further improve the accuracy of the intraoperative heart model built by "virtual touch".

When using manual physical touch to collect surface points, we can only assume the position error for each point is a simple normal distribution with a diagonal covariance matrix, which means error distribution along x,y and z axis is independent from each other. And in reality, this may not be true. With ultrasound virtual touch, we have better knowledge about the error distribution of each point and we can incorporate such prior knowledge into our registration algorithm to correctly minimize the registration error.

To address the cardiac cycle, instead of using 3D registration, we propose a 4D time-space registration procedure between 4D heart model and 4D registration points. 4D heart model is from 4D CT scan which captures a series of 3D heart models through one cardiac cycle. The 4D registration points are captured during operation at different time spot of a cardiac cycle. Both the heart model and points are synchronized with

ECG signals as its time coordinates. This 4D registration make use of the motility of left atrium during registration, this will not only make the registration more accurate but also make the registration points collecting procedure faster and easier. This 4D registration procedure does not introduce any new devices so it is easy to deploy in hospitals quickly.

To reduce the non-homogeneous error that can not be compensated by any global rigid registration algorithm, we added a local non-rigid registration component. It can be viewed as a correction of the pre-operative CT model to the real heart shape during the operation. After the non-rigid registration, the model should be perfectly fit with the intra-operative surface points and will provide accurate navigation for clinicians.

The components of our navigation system then will be illustrated in the following sections. Section 2 shows how we build the intra-cardiac 3D ultrasound catheter and use it to quickly create an intra-operative heart model. Section 4 shows how to do 4D time-space registration for a beating heart. Section 5 shows how to do non-rigid registration after the global registration to further improve the accuracy. Section 6 shows various way we can visualize the combined model to enable intuitive navigation inside heart.

2 Intra-operative Heart Model by Ultrasound "Virtual touch"

To achieve better registration accuracy, we introduce a novel catheter that combines position sensor, ultrasound sensor together with the ablation unit or other treatment devices. This new combined catheter uses "virtual touch" technique to quickly scan the heart surface using ultrasound during the operation and gradually build a intra-operative heart shape model within minutes. It can greatly improve the speed, accuracy and stability of shape registration. More importantly, with thousands of surface points well spread on the heart wall, we can have a realtime intra-operative heart shape. This heart shape does not have a high resolution as CT scan, but it is the real shape of heart during operation while CT scan usually is pre-operative under different breath phases. Later we will see this realtime heart shape can be used to correct pre-operative CT model using our non-rigid registration component.

Currently, navigation systems like Carto Merge from Biosense Webster developed by Siemens requires doctors to manually move a catheter with position sensor to physically touch heart walls during operation to gather intra-operative shape information. This manually touch process is slow and un-reliable. More important, the registration accuracy is directly depend on the quality of intra-operative surface points. A carelessly captured set of surface points by a doctor could generate much worse registration accuracy than a carefully selected and touched set of points by another doctor. This slow, un-reliable and in-consistent system may make the navigation difficult while it is designed to make it easy.

The key idea of our "virtual touch" is to "see" surface points in ultrasound image to capture them other than to move the catheter tip to and physically touch those surface points to capture them. If we think the heart is like a room, then the Carto Merge

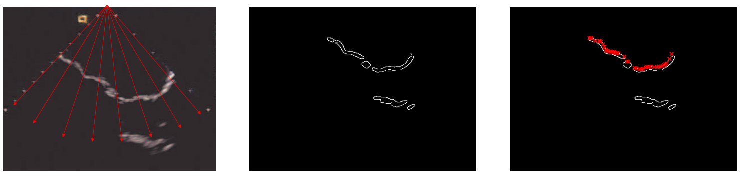

(a) (b) (c)

Figure 4: Detect wall pixels: (a) the input image, red arrows sent out from the catheter center represent the direction we search for edge pixels: for each direction, we start from center and when we meet the first edge pixel, we will stop searching along that direction and move to next direction. (b) the edge detected by canny edge detector. (c) Detection result: red crosses represent the accepted wall pixels. By searching along the red arrows, we can safely discard edges from other chambers of the heart.

catheter is like a blind man who wants to know where the room's wall are. He has to go around blindly until he touches a wall. And then repeats this random walk and touch until he has a rough idea of where the room walls are. Our "virtual touch" catheter on the other hand is like a man who can see. He just needs to go inside the room, stand in the middle and look around. Then he immediately knows where the walls are.

To do this, we need to first automatically detect inner heart wall pixels in ultrasound images (to see the walls) and then reconstruct the 3D coordinates of these pixels (to know where they are). We will go through these steps one by one in the following sections.

2.1 Heart Wall Pixel Detection

First, we need to "see" heart walls in ultrasound image. For computers, it means that we need to have an algorithm to automatically detect wall pixels in ultrasound images.

When the ultrasound frequency, response range, gain and other parameters are tuned accordingly, the heart wall can be seen clearly in ultrasound images. This makes the heart wall pixel detection easier. We first use canny edge detector [2] to detect edge pixels. We usually set the threshold of canny edge detector to a high level because we only want to collect wall pixels with high confidence (clear edge). This is important to ensure the quality of our registration points.

Sometimes, other chambers of the heart can be visible in the far side of the ultrasound image, to avoid including edge pixels of other chambers, we search along a bunch of beams sent out from the ultrasound catheter center as the red arrows shown in Figure 4 (a). When we search along one beam and hit one edge pixel, we accept the pixel as a wall pixel, stop the search along that beam and switch to next beam. Such searching strategy allows us to quickly include all the pixels that are on the wall of the chamber in which the catheter currently is and avoid most wall pixels belongs to other chamber, as shown in Figure 4 (c). More sophisticated contour detection methods could be used here. But we found this light-weight technique works just fine and it is very fast.

2.2 3D Reconstruction with Intracardiac 3D Ultrasound

After we detected heart wall pixels in an ultrasound image, we need to reconstruct the 3D coordinates of them. A 3D ultrasound catheter can make it. In our prototype system, we attached Ascension technology's Microbird tracking sensor onto a Siemens's Acuson intra-cardiac ultrasound catheter to build a 3D intracardiac ultrasound catheter. We use single plane phantom [16] to calibrate the 3D ultrasound catheter. Temperature corrections The calibration will find a matrix *T* and pixel size S_x, S_y. Then the 3D coordinates of any pixel *p(x,y)* in an ultrasound image can be calculated by:

$$P = M_i T \begin{pmatrix} xS_x \\ yS_y \\ 0 \\ 1 \end{pmatrix} \tag{1}$$

where M_i is the direct reading from the magnetic position sensor at the moment the ultrasound image is captured. It's a transformation matrix which gives the position and orientation of the position sensor attached to the ultrasound catheter. S_x, S_y is the size of pixel's width and hight in millimeter. T transforms the 2D pixel coordinate to the 3D coordinate of the position sensor and M_i transforms from the position sensor's coordinate to the transmitter's coordinate which is fixed during an operation. And eventually we get the 3D coordinate P.

2.3 Heart Shape Model Created by "Virtual Touch"

As we can automatically detect heart wall pixels in ultrasound images and reconstruct the 3D coordinates of the wall pixels, the intra-operative heart shape building procedure becomes much easier: Clinicians only need to insert the 3D ultrasound catheter and make the image plane sweep the wall of heart. Our system will automatically capture the video output of the ultrasound catheter and detect wall pixels. The 3D coordinates of those pixels can be immediately calculated using equation 1 as shown in Figure 5. No physical touch is necessary: as long as the ultrasound image plane "touches" the heart wall, our system can capture all the wall points automatically. That's why we call this technique a "virtual touch". It's like a man who can "see" where the walls are and does not need to physically touch walls to locate them. Such strategy can greatly improve the efficiency of the registration.

Noted that this intr-operative shape model can be improved while capturing more and more surface points. During the procedure, clinicians can initially scan a rough model and try to register it with pre-operative high resolution model. Upon the result, further scans can be done to refine the registration in areas where more inconsistency between the two models are found.

2.4 Registration Results and Discussion

We tested the prototype system with phantom models built from a real patient's CT scan. The phantom model's inside cavity has the same shape as the patient's left atrium. During the test the model was submerged in a water tank. We inserted the

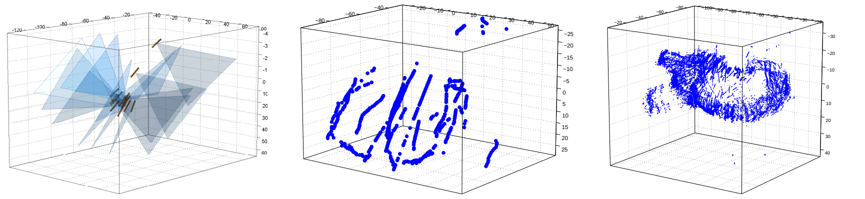

(a) (b) (c)

Figure 5: Virtual Touch: (a) Clinicians only need to move and rotate the 3D ultrasound catheter so that the ultrasound image plane can sweep large portion of the heart. (b) The system can automatically reconstruct the 3D wall points seen by ultrasound images. (c) An example of the heart wall points captured by our system. There are total 12781 wall points from 427 images which is captured within 3 minutes. Noted that by current protocols, a highly experienced clinician may need 30 minutes to capture only 100 surface registration points.

(a) (b) (c)

Figure 6: Phantom model test: (a) the 3D model of a patient's left atrium. (b) the inside hollow model whose cavity has the same shape of the left atrium. (c) the phantom model built by 3D printer with a catheter inserted into it.

3D ultrasound catheter inside the model and captured some wall points. The points then is registered using ICP algorithm to the 3D surface model which is used to build the phantom.

2.4.1 Registration Speed

During the test, we captured 427 ultrasound images within 3 minutes (at 2.5 frames/second) as shown in Figure 5 (c). Image processing (wall pixel extraction and 3D reconstruction) can be done in the same rate. And after 3 minutes, we successfully created a intr-operative shape model with 12871 surface registration points (heart wall points). Comparing to currently move-and-touch protocol which usually needs about 10 minutes for 50-60 points (only achievable by highly experienced clinicians), our method is more than 700 times faster.

As ICP algorithm only takes seconds to find the registration using currently available workstations, the majority of time for registration process is spent to collect registration point. With 700 times faster, the whole registration process time will be greatly shortened. In our case, with 12871 surface registration points, the ICP algorithm still can be done around 1 minute. So the increase of time used by ICP to process more points is negligible comparing to the time saved to collect these points.

2.4.2 Registration Quality

We registered the surface points captured by "virtual touch" to the 3D model from CT. The average distance from registered points to their closest points on surface model is 1.2143mm.

As we can see in Figure 7, there are some outliers in our point set. Those are because of the speckle noise in ultrasound images. We expect there are tens of such outliers exist in our point data set. But given the total number of points in our point set is 12781, these less than 1% outliers can not divert the registration from the true alignment. And with trimmed ICP algorithm [3], the effect of outliers can be easily fixed.

This is a good registration. But the error measurement of closest distance to surface model which is minimized by ICP algorithm may be misleading. It is because the closest point on surface model for a surface point is not its true corresponding point on the surface model. In reality, this true corresponding point usually is not available unless for some manually selected landmark points. In order to get a more accurate measurement of registration quality, we use the average distance from registered points to their true corresponding points on the surface. The true corresponding points are found by manually adjust an automatically found registration to make sure it perfectly fit the surface model. Under this perfect registration, the location of registered points are where they truly should be. Then a new registration will be compare to this registration. The registered points by the new registration is measured against these ground truth locations of surface points. And its average will be our measurement of registration error in the following tests.

Our registration systems actually sample the intra-operative heart shape using surface points and register this sampled surface shape to pre-operative full shape model (CT). Because the intra-operative sampled heart shape only have partial information, the loss of information will introduce ambiguity for registration. A good registration system can greatly reduce such ambiguity so that it has good chance to find true registration. David Simon [23] showed us given a shape, how to determine the best locations to sample it to maximize the stability and accuracy of registration. But in reality, before registration we don't know where our catheter is inside heart. Then we can't move the catheter to the desired locations to sample the shape. Instead, we can only random sample the shape. With only a few samples of the shape, registration may have a lot ambiguity or local minimums. As we add more random samples, we can reduce ambiguity or local minimums so that registration algorithm can have a better chance to converge to the true registration and eventually improve its accuracy. Now we would like to know the ***lower bound of*** how many random samples we need to ensure a given stability goal.

We designed a stability test with our phantom data. We generated 100 random initial alignments: ± 30 degree of rotation along x, y and z axis, and ± 5 millimeter translation from ground truth registration. And we randomly sub-sampled our 12781

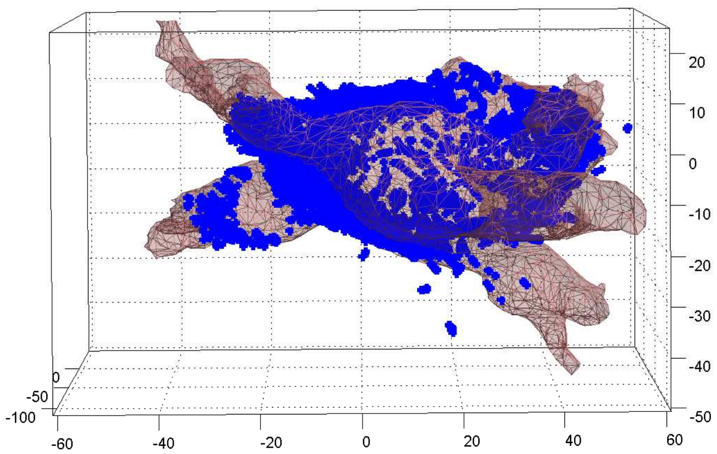

(a)

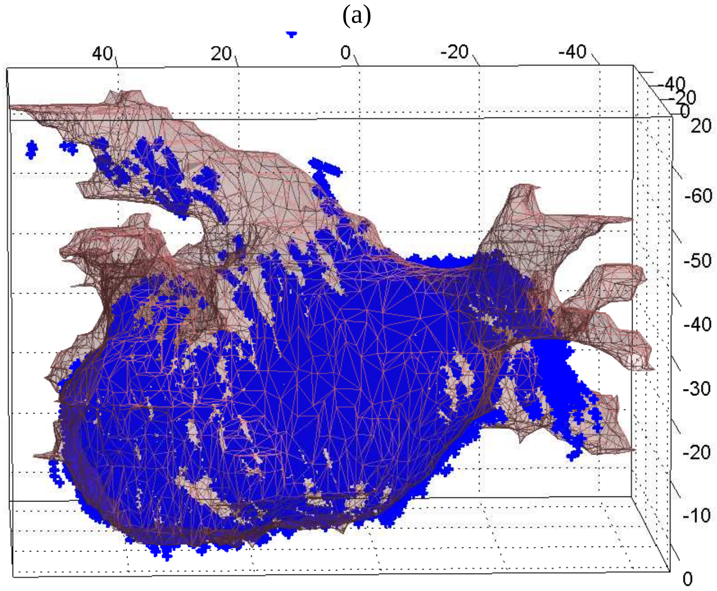

(b)

Figure 7: Registration Result: average distance to closest point on surface model is 1.2143mm.

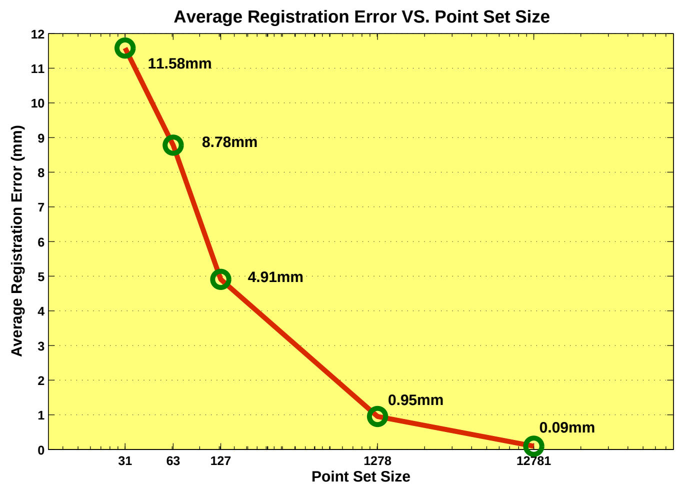

(a)

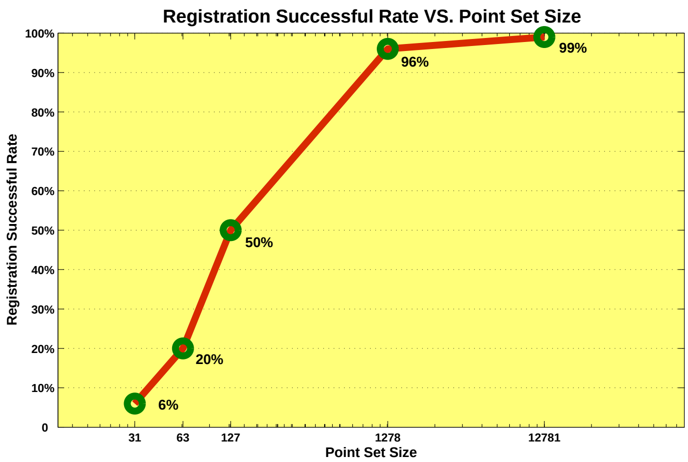

(b)

Figure 8: Stability Test Result: (a) Average distance to true registration of 5 point sets. (b) Successful rate of registration with 5 point sets. We define a registration is successful if average distance of each registered point to its location in true registration is less than 1mm

surface registration points down to four other point sets each having 1278, 127, 63 and 31 points. These points are well spread over the left atrium. With these five sets of sample points we do registration from all the 100 random initial alignments. After each registration, we calculate the average distance of points from this registration to the ground truth registration and then the average distance of all 100 tests. In this test we want to know

1. How registration accuracy is affected by number of surface points?
2. What is the probability of finding true registration with a given number of surface points?
3. What is the minimum number of surface points we need to capture in order to achieve a reasonable chance of finding the true registration?

Result of our test is shown in Figure 8 (a).

To show how likely each point set will register to the ground truth, we also calculated the registration successful rate over 100 tests. We define a registration is success if the average distance from registered points to its location in ground truth registration is less than 1mm. Result is shown in Figure 8 (b).

It is shown in Figure 8 that to achieve 95% stability, we need to random sample more than 1000 points over the left atrium surface. This number is much higher than any current available registration systems can achieve, which suggests a sample set of around 50 - 150 points. As shown in our test result, with such few samples of the shape, registration only has a successful rate of about 50% or less. The reason all these systems failed such stability requirement is it is too time-consuming (may need hours) for doctors to physically touch catheters to 1000 locations on heart wall with these systems. But with “virtual touch”, to capture ten thousand points will not take 3 minutes. This ensures a 99% chance to get a true registration with only a rough initial alignment. With such superior stability, clinicians can be much more confident about the registration found with “virtual touch” while with currently available commercial systems, doctors must face the fact that the registration only has a 50% chance to be correct.

3 ”Virtual Touch” Model with Ultrasound Image Thickness Correction

To reconstruct 3D heart surface points with “Virtual Touch”, in previous section we use simple edge detection algorithm to find first edge pixel in ultrasound images from transducer’s center corresponding the first reflected sound. With a position sensor on the ultrasound catheter 3D coordinates of those pixels can be computed. This method assumes ultrasound image plane is infinitely thin so that all the edge pixels detected on the ultrasound image are thought to be at the image plane. But in reality ultrasound image plane has thickness, thus introduces noticeable error when reconstructing the 3D coordinates of heart wall pixels. Eventually it will bring error to the intra-operative 3D heart model.

3.1 Error Caused by Image Plane Thickness

Figure 9 (a) shows an ultrasound image plane (bold black line) with finite thickness (thin black lines) intersect an object surface (horizontal blue line). Because the image plane is not perpendicular to the object surface, at point a, part of the image plane first hits the object surface and reflects some ultrasound energy. o' is where the center image plane hits the object surface and reflects energy. Eventually, the object surface in ultrasound image will be a wide band (Figure 9 (b)), *not* an infinitely thin line as it should be with zero thickness image plane. In this case, if we just detect the first edge pixel from the transducer in ultrasound image (represents the first reflection of sound waves) as where the surface is and assume it is in the infinitely thin image plane, o will be taken as a point on the object surface while the real 3D point on the object surface should be a.

This error is proportional to the ultrasound image plane's thickness at the depth o. Thickness of an intra-cardiac ultrasound catheter's image plane ranges from 3 to 6mm. Navigation error acceptable to doctors is around 2mm or less. Also it is related the intersecting angle between the ultrasound image plane and the object surface. If they intersect at a right angle (perpendicular to each other), and the object surface is flat within 3-6mm range from the intersection point, even assuming the image plane is infinitely thin, it still will not introduce errors. While if the intersection angle is smaller, the error will be larger. Such error cause by thickness of image plane has been observed[16]. But in [16] only suggestion of avoiding intersecting with small angle is given, no solution to correct this error has been provided.

To address such error from ultrasound image plane thickness, we first propose a method to measure the thickness of an ultrasound image plane in section 3.2. And we provide an algorithm to correct 3D surface points errors with measured thickness information (section 3.3) and register (section 3.4) the corrected points with pre-operative 3D heart surface models. A phantom model test and its result analysis will be presented in section 3.5 to verify the improvement with our algorithm.

3.2 Ultrasound Image Thickness Measurement

Thickness of ultrasound image plane is also called the ultrasound beam width. It is not uniform everywhere and can be thought as a function of depth (distance from the ultrasound transducer):

$$T = f(Depth)$$

We assume the image plane thickness (beam width) is the same for any two locations who have the same distance to the ultrasound transducer's center.

Ultrasound image plane thickness can be measured by carefully built phantom models [18][24]. The basic idea is to intersect the ultrasound image plane with a flat surface at an angle of 45 degree. In that case, the width of the band in ultrasound image equals to the thickness of the image plane at the depth. Then either move the ultrasound transducer up and down or use multiple parallel surfaces to measure the distance at different depth. To precisely measure image thickness those methods need carefully built

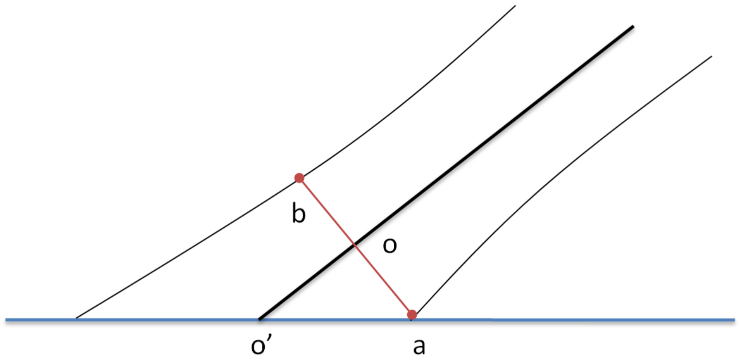

(a)

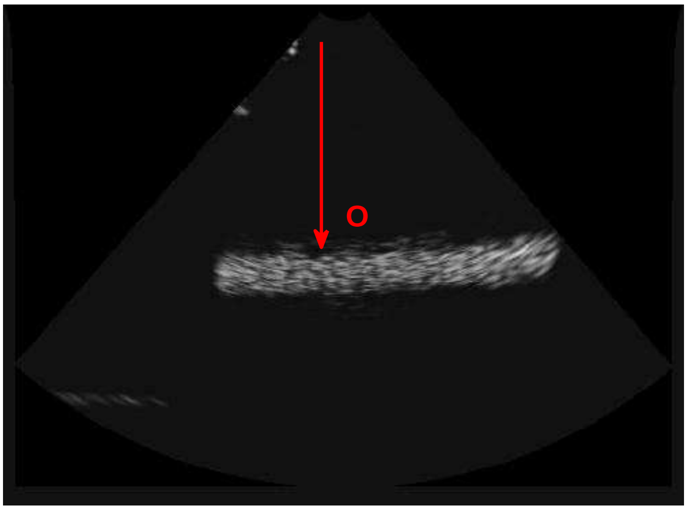

(b)

Figure 9: Surface intersect with ultrasound image plane with finite thickness

models and accurate movement of transducers. Usually it can only be achieved with special devices and manufacture capabilities.

In this paper we introduce an algorithm that can reduce many restrictions of phantom model of those methods to as simple as a single slope surface with any angle (0-90) to a flat water tank bottom. It is easy to build and no special devices are needed.

3.2.1 Phantom Model Setup

Our method requires only a single slope on a flat surface (a flat water tank bottom will do) as shown in Figure 11 (a). Our model has an extended flat surface only because the material of our model has a better visibility in ultrasound than the water tank bottom. There is no restriction to the slope's angle α, but an angle close to 45 degree is suggested. Usually it can be built by cut out wedge shape piece of plastic and then measure the slope angle. No need to build a slope precisely at a certain angle. Thus the model is easy to build.

We use a clamp to hold the ultrasound catheter (Figure 11 (a) highlighted by red lines) so that the ultrasound image plane (blue plane) is perpendicular to the water tank bottom. It can be verified by rotating the catheter along its proximate direction until the white band in ultrasound image generated by the tank bottom is at its thinnest. This can be done by manually rotating the catheter back and forth and inspect the ultrasound image to find the thinnest band. At this time, the thin straight line in ultrasound image representing the water tank bottom is called our "*reference line*". Later we will need it to compute thickness.

Now we can slide the slope into the image plane. As we move the slope back and forth, the white band representing the slope surface should sweep across the ultrasound image at different depth. We capture all these ultrasound images for later steps. Noted that we need to sweeps most part of the ultrasound image multiple times to make sure we have enough samples at various depth.

3.2.2 Compute the Thickness Function

Consider any one of the ultrasound images captured during this procedure as shown in Figure 11 (b). It is a general case of the intersection: the blue plane $aba'b'$ is the slope surface. The yellow vertical plane $bcb'c'$ is the ultrasound image plane. It is perpendicular to the flat surface where triangle $\triangle abc$ lies. The ultrasound image we will see is shown as Figure 11 (c). The white band is the reflection of the slope surface. The white thin line is the reference line reflected by the flat bottom.

Because the image plane at point O has a thickness of $ac + a'c'$, and it intersect with the slope plane at aa', in the ultrasound image, we should see a belt centered at bb' with a vertical thickness of cc'. As shown in Figure 11 (c).

The thickness of the belt in ultrasound image cc' can be measured. We define it as w. Then the length of oc is $w/2$. In $\triangle odc$, $\angle ocd$ is a right angle because we have calibrated the ultrasound image plane $bcb'c'$ to be perpendicular to the flat bottom surface abc. And $\angle odc$ is the slope angle $alpha$ which is known (it can be measured when building the model). Then the length of cd is:

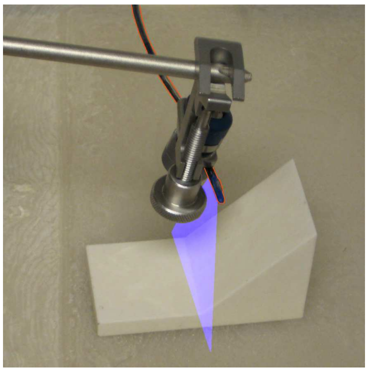

(a)

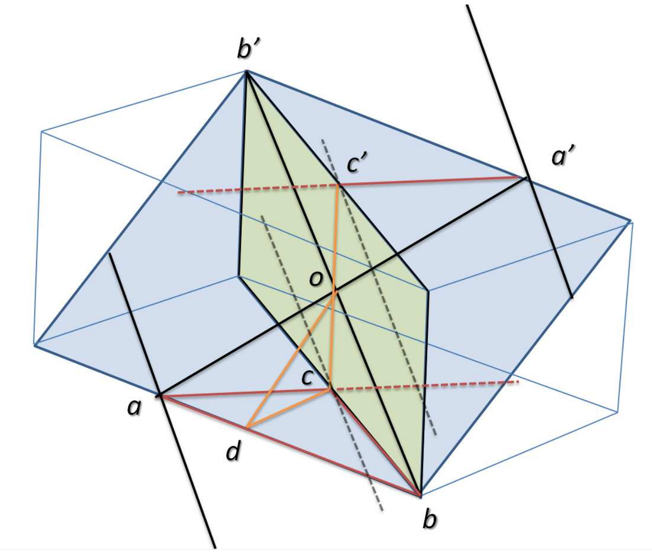

(b)

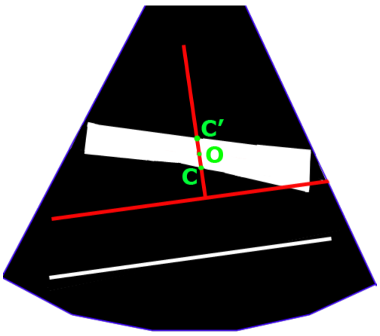

(c)

Figure 10: Measure thickness of an ultrasound image plane

$$|cd| = \frac{w}{2} ctan\alpha \tag{2}$$

Also in $\triangle obc$, $\angle ocb$ is a right angle and $\angle obc$ can be measured in ultrasound image automatically: line ob can be detected in ultrasound image and line cb is parallel to the reference line. Then the $\angle obc$ can be computed. We define it as $beta$. Then the length of cb can be written as:

$$|cb| = \frac{w}{2} ctan\beta \tag{3}$$

Now we look at $\triangle abc$. Because ac is perpendicular to the image surface, so $\angle acb$ is a right angle. And cd is perpendicular to ab so $\angle cdb$ is also a right angle. Then we can have:

$$\frac{|cb|}{|db|} = \frac{|ac|}{|cd|}$$

and then

$$|ac| = \frac{|cb||cd|}{|db|}$$

replacing $|cd|$ and $|cb|$ with equation (2) and equation (3), and $|db| = \sqrt{|cb|^2 - |cd|^2}$, we have:

$$|ac| = \frac{w}{2} \cdot \frac{1}{\sqrt{tan^2\alpha - tan^2\beta}}$$

And the thickness of the image plane is two times of $|ac|$ which is:

$$Thickness = w \cdot \frac{1}{\sqrt{tan^2\alpha - tan^2\beta}} \tag{4}$$

If the model is built with a slope angle α of 45 degree. This simplifies equation (4) because $tan\alpha = 1$ in this case. And if the ultrasound image plane and the slope surface is intersect carefully to make angle β close to zero, then $beta = 0$ and $tan\beta = 0$ too. Then equation (4) is further simplified to

$$Thickness = w$$

This is exactly what [18][24] did. Now we can see these models are special case of our general thickness measuring algorithm. The point is that the cost to simplify equation (4) is to have special devices to precisely build slope model and control the intersection angle between ultrasound image plane and the model. In our case, since $alpha$ can be measured after the slope model is built and $beta$ can be automatically measured in ultrasound image (details will be shown below), almost any lab without special device can use our method to measure ultrasound image thickness.

Now the only problem is how to automatically measure $beta$ and the width w of the white belt in ultrasound image. As shown in Figure 11 (a) is the ultrasound image with slopped surface as a belt in it. First by applying a smoothing filter and a threshold for the image, we can get a clear white band shown as in Figure 11 (b). Although we can directly measure the thickness of the belt at different locations, because there is a lot of noise, the thickness tend to be inconsistent. To reduce this noise, we fit two second order polynomial curve to the upper and lower boundary of the belt as shown in Figure 11 (c). The reason we fit two second order polynomial curves instead of two straight lines is that within the band, the depth (distance to transducer) is not the same for every point. Thus the width of the band should not be the same. Given the fact that the band could be in any angle and the thickness of ultrasound image plane is not a linear function of depth, the shape of the band could be very complex. But practically a second order curve should be enough to capture this complexity and in the mean time reduce errors caused by poor ultrasound image quality.

Suppose the curve of upper bound and lower bound of the band can be written as:

$$\begin{aligned} y_{upper} &= p_2 x^2 + p_1 x + p_0 \\ y_{lower} &= q_2 x^2 + q_1 x + q_0 \end{aligned} \tag{5}$$

The center of the band which should be a straight line which can be approximated by

$$y = \frac{p_1 + q_1}{2} x + \frac{p_0 + q_0}{2} \tag{6}$$

With the center line function of the band, we can compute the angle between it and the reference line: $beta$. Reference line will stay static for all ultrasound images so its line function only need to be measured for once. Now we have $beta$.

The width w of the band at a given point is defined as the length along the direction perpendicular to the reference line. The function of the reference line is know and we write it as:

$$y = r_1 x + r_2 \tag{7}$$

Suppose we want to measure the width at a point (x_0, y_0) which is at the center line of the white band. Then the function of a line perpendicular to the reference line through (x_0, y_0) is:

$$y = \frac{1}{r_1}(x - x_0) + y_0$$

Intersecting points of this line with the upper bound and lower bound of the band can be easily computed then. And the distance between the two intersecting points is w. Now we have w.

Put the measured w and $beta$ into equation (4) we can compute the thickness at the point (x_0, y_0). The depth of point (x_0, y_0) can be easily computed as the transducer center is known (during 3D ultrasound catheter calibration). Then we have one sample of thickness at the depth.

If the we carefully setup the ultrasound catheter so that the reference line is parallel to the x-axis of the ultrasound image, the w can be simply computed by this formula:

$$w = (p2 - q2)x^2 + (p1 - q1)x + p0 - q0$$

(a) (b) (c)

Figure 11: Measure ultrasound image plane thickness with phantom model.

Now we know how to compute the thickness for a given ultrasound image at a point of (x_0, y_0). We can then repeat these steps to other points in the same image, and other points in other images. By measure more samples at various depth, we can accumulate enough samples to interpolate the curve of image thickness VS depth.

In Figure 12 is 3D views of the result of our ultrasound image plane's thickness. It shows that the region near the image center and far away from image center tends to be thicker while the region in the middle (focus zone) tends to have minimum thickness. This is just as we expected because most ultrasound device manufacturer calibrate their ultrasound sensors so that the middle field has minimum thickness and thus gives clearest image and less errors. From this result we can see, to maximize the accuracy of "Virtual Touch" points we need to scan points with the middle region of the image. And based on this thickness measurement, we can correct 3D reconstruction error caused by ultrasound image thickness and achieve better accuracy.

3.3 Image Thickness Correction

As stated in section 3.1, finite thickness of ultrasound image plane can cause error for 3D coordinate reconstructed for wall pixels. With the measured thickness of the image plane, we can correct this error.

Figure 13 (a) shows an ultrasound image plane (yellow surface). With 3D ultrasound catheter, the normal of ultrasound image plane N_{img} is known. t is the transducer's center which is also known with 3D ultrasound catheter. Suppose o is a detected point at the first edge from transducer's center, then there are two possible object surface point which can generate the edge at o in ultrasound image: a and b. If the thickness of the image plane at o is T, a and b are $\pm T/2$ away from o along the image normal direction N_{img}.

Suppose we know the normal of the object surface N_{obj} near o, we can draw a plane with the object surface normal through b as the red plane in Figure 13 (b). As we can see this plane intersect with line segment ot which means o is not the first edge pixel in the ultrasound image from the transducer. Then it contradicts with the fact that o is detected as the first edge from the transducer. So b can not be on the object surface. Similarly we can create a plane through a with object surface normal as the green plane shown in Figure 13 (c). It doesn't intersect with line segment ot. So a should be the true point on the object surface. By applying this logic to every 3D object surface point,

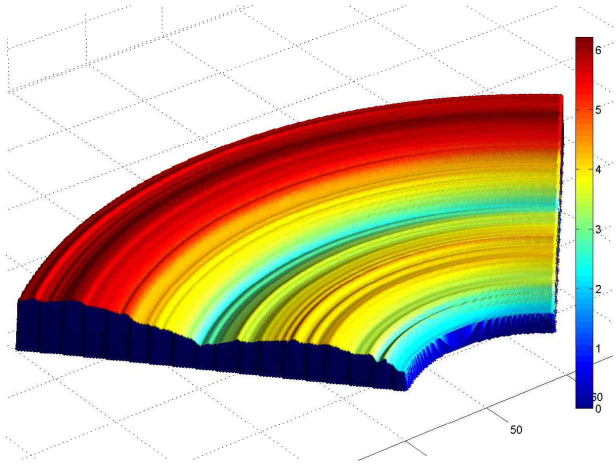

(a)

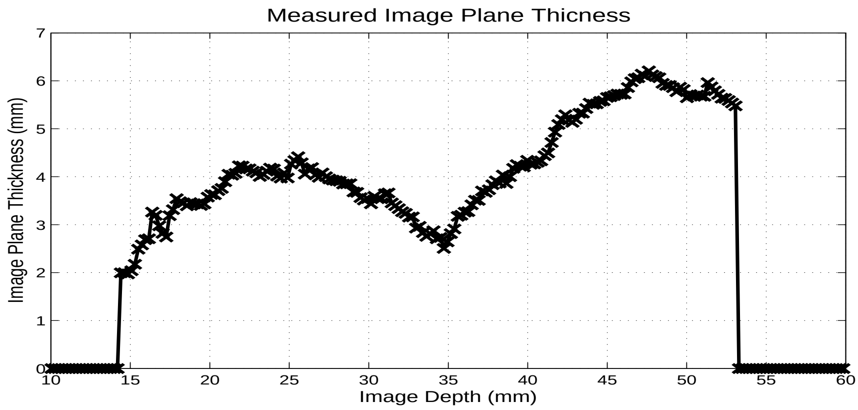

(b)

Figure 12: Measured thickness of ultrasound image plane. (a) 3D visualization of the thickness of an ultrasound image. (b) The thickness function we measured. X-axis is depth (distance from transducer) and Y-axis is thickness (beam width). Depth with zero thickness means no sample has been captured at that depth.

we correct errors caused by ultrasound image thickness.

To write the correction procedure in a mathematical manner, we first define the coordinate of the detected edge point $o = (x_o, y_o, z_o)$, and transducer's center $t = (x_t, y_t, z_t)$. The normal of the image plane is $N_{img} = (x_{img}, y_{img}, z_{img})$ which is a unit vector. The normal of the object near o is $N_{obj} = (x_{obj}, y_{obj}, z_{obj})$ which is also a unit vector. The image plane thickness at the depth of o is T.

Then two possible real object surface points are

$$\begin{aligned} a &= o + \tfrac{T}{2} N_{img} \\ b &= o - \tfrac{T}{2} N_{img} \end{aligned} \tag{8}$$

The two plane through a and b with normal of N_{obj} then are

$$\begin{aligned}(p-a)\cdot N_{obj}=0\\(p-b)\cdot N_{obj}=0\end{aligned} \tag{9}$$

The line segment ot's function is:

$$p=o+r(t-o);\quad 0\leq r\leq 1 \tag{10}$$

Here r is a parameter of the line. Combining equation (10), (9) and (8), we can find the parameter r for the intersection of the two planes with the line segment:

$$\begin{aligned}r_a=\tfrac{T}{2}N_{img}\cdot N_{obj}/((t-o)\cdot N_{obj})\\r_b=-\tfrac{T}{2}N_{img}\cdot N_{obj}/((t-o)\cdot N_{obj})\end{aligned} \tag{11}$$

r_a is the intersecting point's parameter for plane that through point a. r_b is for the plane through point b. If r_a is within the range of $[0,1]$, it means plane through point a intersects with line segment ot. It contradicts with the fact that o is detected as the first edge point. Then a is not the true object surface point, and b must be the true point. And vise verse.

With equation (11) we can determine which of the two possible points are true surface points and then correct the reconstructed 3D coordinate of detected surface pixel o. Now we only need to know the object surface normal near point o: N_{obj}. Noted that without knowing the registration, we can not know exactly which part of the object the true surface point should be, then we can not know the N_{obj}. But it can be roughly estimated by first registering the un-corrected 3D points to the 3D surface model of the object (usually from pre-operative CT or MRI). After registration, we take the normal of the closest point on the surface model to o as the estimated object surface normal N_{obj}. Because we only use this normal to determine which one of a and b is the true object surface point (r is in $[0,1]$ or not), a rough estimation will work.

3.4 Registration with Image Thickness Correction

If we capture surface registration point one by one with physical touch, each point is treated independently. We can assume the position of each point's coordinate has the same normal error distribution of $N(0,\sigma)$ and then we can use standard ICP algorithm to find space registration which minimizes the error or maximizes the probability of registered surface points given the error distribution model. All previous result we shown are using this registration method.

When we use ultrasound virtually touch to collect surface registration points, however the error distribution changes. Pixels extract from different regions of the ultrasound image tend to have different error distribution. Points from same ultrasound image share some similarity in error distribution. Thus the registration algorithm should be modified accordingly.

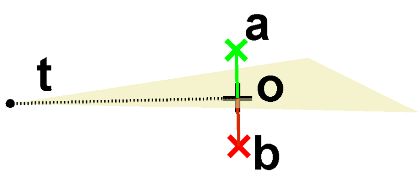

(a)

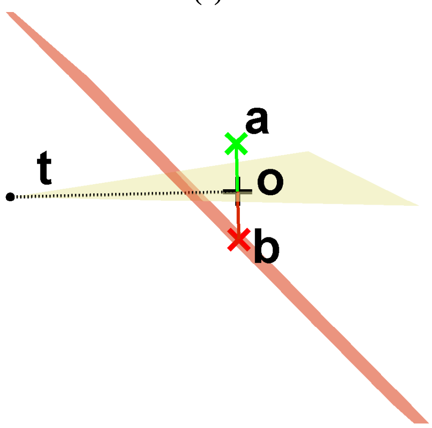

(b)

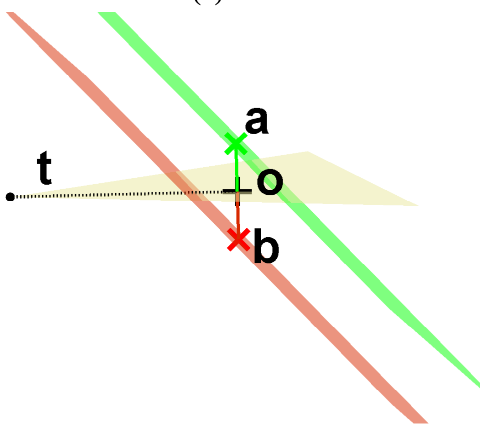

(c)

Figure 13: 3D position correction

3.4.1 3D Position Error Model of "Virtual Touch" Points

In previous section, we analyzed the error distribution We want to know the 3D position error distribution of a wall point p whose image coordinate is $X = (x, y, 0, 1)^T$. After thickness correction, it is $X = (x, y, z, 1)^T$. This correction is based on thickness measured with error. The image center's rotation and translation matrix given by the position sensor reading is R and T. We know there are errors in these position sensor readings and we want to find how these errors affect the final reconstructed 3D position of "Virtual Touch" points. We use C to represent the 3D ultrasound calibration matrix then the 3D coordinate of point p can be computed as:

$$P = R \cdot C \cdot X + T \tag{12}$$

Rotation and translation matrix are $\Delta R \cdot R$ and $T + \Delta T$ to represent readings with error. Similarly the error also exists for the wall pixel's position after correction as we stated in the previous section: $X + \Delta X$. With errors, Equation 12 becomes:

$$\hat{P} = \Delta R \cdot R \cdot C \cdot (X + \Delta X) + T + \Delta T$$
$$\hat{P} = \Delta R \cdot R \cdot C \cdot X + \Delta R \cdot R \cdot C \cdot \Delta X + T + \Delta T \tag{13}$$

Then the error of the reconstructed 3D position of point p is:

$$\Delta P = (\Delta R - I) \cdot R \cdot C \cdot X + \Delta R \cdot R \cdot C \cdot \Delta X + \Delta T \tag{14}$$

Error from Detected Wall Pixels

First we need to define the error distribution of a corrected wall pixel's coordinate. As we have stated in the previous section, it is based on the thickness of the image plane at the wall pixel location. This thickness is measured by the method we given in section **??**. We know the measured thickness has an error distribution of:

$$\Delta X \sim N(0, \Sigma_X); \tag{15}$$

where Σ_X is the variance of the measured error.

Rotation Error from Position Sensor

We define the rotation error along x, y and z axes are $\Delta\theta_x, \Delta\theta_y, \Delta\theta_z$, the ΔR can be written as:

$$\Delta R = \begin{pmatrix} r_{11} & r_{12} & r_{13} & 0 \\ r_{21} & r_{22} & r_{23} & 0 \\ r_{31} & r_{32} & r_{33} & 0 \\ 0 & 0 & 0 & 1 \end{pmatrix}$$

$$r_{11} = cos(\Delta\theta_z)cos(\Delta\theta_y)$$
$$r_{12} = -sin(\Delta\theta_z)cos(\Delta\theta_x) + cos(\Delta\theta_z)sin(\Delta\theta_y)sin(\Delta\theta_x)$$
$$r_{13} = sin(\Delta\theta_z)sin(\Delta\theta_x) + cos(\Delta\theta_z)sin(\Delta\theta_y)cos(\Delta\theta_x)$$
$$r_{21} = sin(\Delta\theta_z)cos(\Delta\theta_y)$$

$$
\begin{aligned}
r_{22} &= cos(\Delta\theta_z)cos(\Delta\theta_x) + sin(\Delta\theta_z)sin(\Delta\theta_y)sin(\Delta\theta_x) \\
r_{23} &= -cos(\Delta\theta_z)sin(\Delta\theta_x) + sin(\Delta\theta_z)sin(\Delta\theta_y)cos(\Delta\theta_x) \\
r_{31} &= -sin(\Delta\theta_y) \\
r_{32} &= cos(\Delta\theta_y)sin(\Delta\theta_x) \\
r_{33} &= cos(\Delta\theta_y) * cos(\Delta\theta_x) \qquad (16)
\end{aligned}
$$

Given the linear approximation:

$$
\begin{aligned}
sin(\theta) &\approx \theta \\
cos(\theta) &\approx 1
\end{aligned}
$$

when θ is small, we can rewrite equation (16) as:

$$
\begin{aligned}
r_{11} &= 1 \\
r_{12} &= -\Delta\theta_z + \Delta\theta_y\Delta\theta_x \\
r_{13} &= \Delta\theta_z\Delta\theta_x + \Delta\theta_y \\
r_{21} &= \Delta\theta_z \\
r_{22} &= 1 + \Delta\theta_z\Delta\theta_y\Delta\theta_x \\
r_{23} &= -\Delta\theta_x + \Delta\theta_z\Delta\theta_y \\
r_{31} &= -\Delta\theta_y \\
r_{32} &= \Delta\theta_x \\
r_{33} &= 1 \qquad (17)
\end{aligned}
$$

Since $\Delta\theta_x, \Delta\theta_y$ and $\Delta\theta_z$ are small (around 1 degree), we can further approximate ΔR by keeping only the linear part of it:

$$
\Delta R \approx \begin{pmatrix} 1 & -\Delta\theta_z & \Delta\theta_y & 0 \\ \Delta\theta_z & 1 & -\Delta\theta_x & 0 \\ -\Delta\theta_y & \Delta\theta_x & 1 & \\ 0 & 0 & 0 & 1 \end{pmatrix} \qquad (18)
$$

We define $R \cdot C \cdot X = (P_x, P_y, P_z, 1)^T$. Then the first term in equation (14) becomes:

$$
(\Delta R - I) \cdot (P_x, P_y, P_z, 1)^T = \begin{pmatrix} -\Delta\theta_z P_y + \Delta\theta_y P_z \\ \Delta\theta_z P_x - \Delta\theta_x P_z \\ -\Delta\theta_y P_x + \Delta\theta_x P_y \\ 1 \end{pmatrix} \qquad (19)
$$

Similarly we define $R \cdot C \cdot \Delta X = (\Delta P_x, \Delta P_y, \Delta P_z, 1)^T$, the second term in equation (14) becomes:

$$\Delta R \cdot (\Delta P_x, \Delta P_y, \Delta P_z, 1)^T =$$
$$\begin{pmatrix} -\Delta\theta_z \Delta P_y + \Delta\theta_y \Delta P_z + \Delta P_x \\ \Delta\theta_z \Delta P_x - \Delta\theta_x \Delta P_z + \Delta P_y \\ -\Delta\theta_y \Delta P_x + \Delta\theta_x \Delta P_y + \Delta P_z \\ 1 \end{pmatrix}$$

Given $\Delta\theta_x, \Delta\theta_y, \Delta\theta_z, \Delta P_x, \Delta P_y, \Delta P_z$ are small, we keep only the linear part of the above formula:

$$\begin{pmatrix} \Delta P_x \\ \Delta P_y \\ \Delta P_z \\ 1 \end{pmatrix} \tag{20}$$

Finally we represent ΔT as $(\Delta T_x, \Delta T_y, \Delta T_z, 1)^T$, and replace the terms in equation (14) with equation (19) and equation (20), then we have:

$$\Delta P = \begin{pmatrix} -\Delta\theta_z P_y + \Delta\theta_y P_z \\ \Delta\theta_z P_x - \Delta\theta_x P_z \\ -\Delta\theta_y P_x + \Delta\theta_x P_y \\ 1 \end{pmatrix} + \begin{pmatrix} \Delta P_x \\ \Delta P_y \\ \Delta P_z \\ 1 \end{pmatrix} + \begin{pmatrix} \Delta T_x \\ \Delta T_y \\ \Delta T_z \\ 1 \end{pmatrix} \tag{21}$$

Because $\Delta\theta_x, \Delta\theta_y, \Delta\theta_z$ are independent random variables following a normal distribution of $N(0, \sigma_\theta)$. The first term of equation (21) follows a normal distribution of $N(0, \Sigma_\theta)$ and

$$\Sigma_\theta = \begin{pmatrix} \sigma_\theta(P_y + P_z) & 0 & 0 \\ 0 & \sigma_\theta(P_x + P_z) & 0 \\ 0 & 0 & \sigma_\theta(P_x + P_y) \end{pmatrix} \tag{22}$$

Wall pixel's position error ΔX follows a normal distribution of $N(0, \Sigma_X)$. Then the second term of equation (21) follows a normal distribution whose mean value is still 0, and standard deviation is:

$$\Sigma'_X = R^T \cdot C^{-1} \cdot \Sigma_X \cdot C \cdot R \tag{23}$$

Translation Error from Position Sensor

The translation error from position sensor ΔT also has a normal distribution of $N(0, \Sigma_T)$. Because the x, y and z component of ΔT are independent with each other and the error distributed in these 3 axes are the same. Then we have:

$$\Sigma_T = \begin{pmatrix} \sigma_T & 0 & 0 \\ 0 & \sigma_T & 0 \\ 0 & 0 & \sigma_T \end{pmatrix} \tag{24}$$

Combining equation (22), (23), and (24) the error of the reconstructed 3D point ΔP follows a normal distribution $N(0, \Sigma_P)$ where:

$$\Sigma_P = \Sigma_\theta + \Sigma'_X + \Sigma_T \tag{25}$$

3.4.2 Registration Algorithm with "Virtual Touch" Points

Because the error distribution model of surface registration point has been changed, the registration algorithm need to be changed accordingly.

Registration algorithm is trying to maximize the probability of $F(P)$ and C where P is the surface registration point set, $F()$ is the current registration function, and C is the CT heart model. If we assume the error distribution function is a normal distribution, to maximize the probability equals to minimize the distance:

$$\arg\min_{F} \sum_{i=1}^{m} (F(p_i) - C_{p_i})^T \Sigma_{p_i}^{-1} (F(p_i) - C_{p_i}) \tag{26}$$

where m is the number of points in P, p_i is the i'th point in point set P, C_{p_i} is the corresponding point of p_i on heart model C. Σ_{p_i} is the covariance matrix for point p_i as defined in Equation (25). In Equation (26), the distance is weighted by $\Sigma_{p_i}^{-1}$, so those points that have larger Σ_{p_i} (larger errors) will be weighted down accordingly. Points that are captured more accurately will have larger weight in the sum of distance. And since the Σ_{p_i} is not diagonal, the correlation of different axes have been considered as well.

The original ICP algorithm can be thought as a simplified version of our registration algorithm which has a single diagonal Σ_p for all the points.

The final registration for "virtual touch" points will be:

1. Reconstruct 3D position of wall pixels.
2. Using ICP to find an initial registration for estimate of intersecting surface normal for each image plane.
3. Correct 3D position of wall pixels using estimated object surface normal.
4. Register the corrected 3D "virtual touch" points to surface model using equation (26).

3.5 Experiments and Results

3.5.1 Phantom Model

We use a simple shape phantom model as shown in Figure 14 (a). Because its shape only consists of several flat surfaces and is not rotational symmetric, it will not introduce any registration difficulties caused by the shape itself. This will make it easier to evaluate the improvement of our algorithms. The 3D surface model is shown in Figure 14 (b).

3.5.2 Registration Error Measurement

Most common way to measure registration error is to use the average distance from registered points to their closest surface points. ICP algorithm actually tries to minimize such measurement. The problem is that it is usually smaller than the distance

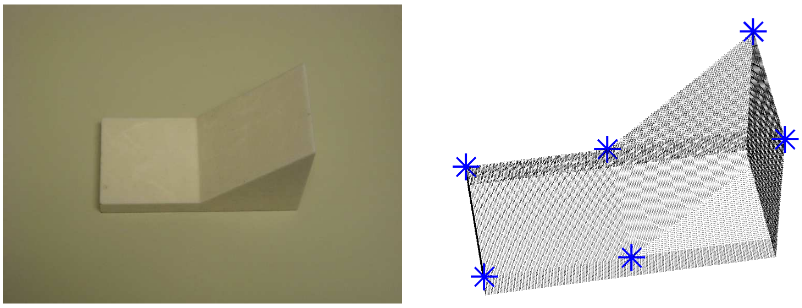

(a) (b)

Figure 14: Phantom model in registration test: (a) the model (b) its 3D model

from the registered points to their true correspondence on object surface. In this case, such error measurement could be misleading.

Here we use a separated set of points called evaluation point set whose corresponding points on object surface are known, as shown in Figure 14 (b) the blue stars. During the test, we will first use 3D ultrasound catheter to scan the model to capture surface points for registration. Also we use a catheter whose tip is tracked by a 3D position sensor to touch those blue points as shown in Figure 14 (b) and record their coordinates as our evaluation points. Then we do the registration with only the surface points scanned by ultrasound catheter. After registration, we apply the transformation matrix found by registration to evaluation points and measure how far they are from their corresponding points on the surface model.

This is exactly what doctors want to know for medical navigation systems that after registration when they maneuver an instrument to a location as shown by the navigation system, how far it is from the real location they want to go. All the registration error shows in our result will use such error measurement.

3.5.3 Accuracy Improvement And Intersecting Angles

As we have already shown, the error caused by ultrasound image plane thickness is related to the intersecting angle of the image plane and the object surface. If the image plane is perpendicular to the object surface (90 degree), there will be no error (caused by image thickness). Smaller the intersecting angle is, larger the error will be. To understand how the intersecting angle will affect registration error and how our thickness correction algorithm can help, we will do a series of tests.

First we scan the phantom model with ultrasound image plane with various intersecting angles (0-90). Then we sample all those images to form several subset of ultrasound images each with a different average intersecting angles.

For example one subset may have many images whose average intersecting angle is 80 degree and another set has an average intersecting angle of 40 degree. We expect that registration error with un-corrected points from first set will have less error than those from the second set. After thickness correction, they should all have improvements and both sets should have similar errors. The relation among expected registration errors

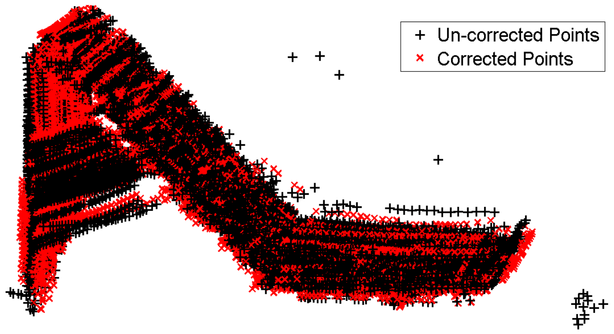

(a)

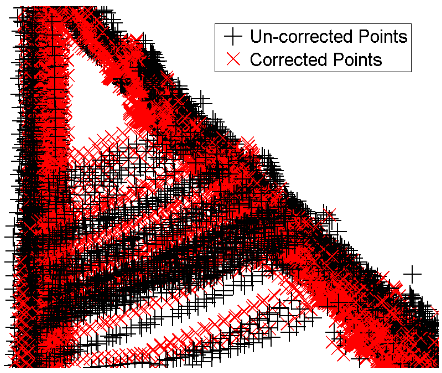

(b)

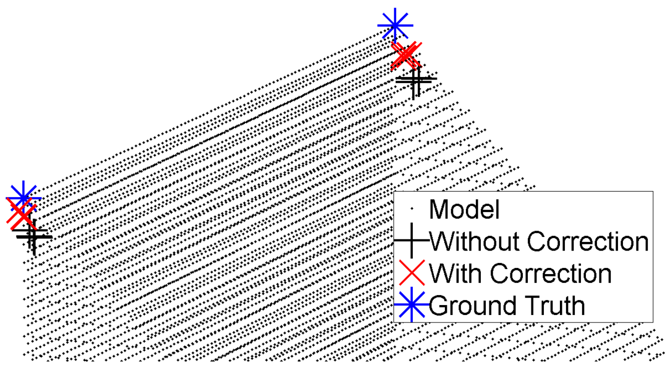

(c)

Figure 15: Corrected (red x) and un-corrected (black +) surface registration points and result of evaluation points

should be:

$$P^{40}_{un-corrected} > P^{80}_{un-corrected} > P^{40}_{corrected} = P^{80}_{corrected} \tag{27}$$

where $P^{x}_{un-corrected}$ means registration error with un-corrected points from a subset whose average intersecting angle is x and $P^{x}_{corrected}$ means registration error with corrected points.

3.5.4 Result and Analysis

Figure 15 (a) and (b) shows the overall and zoomed in view of thickness corrected (red x) and un-corrected (black +) surface points. We can see that the corrected points have a tighter fit than the un-corrected ones. After registration, we can see the result of evaluation points in Figure 15 (c), the result from corrected points (red x) are closer to ground truth (blue *) than un-corrected points (black +).

Quantitative results are shown in Figure 16. X-axis is average intersecting angle. Y-axis is registration error. Blue line with green x's is for the un-corrected points. Red line with blue circles is for the points corrected using our algorithm. Through the spectrum, our corrected points consistently achieves better registration accuracy than points without thickness correction. This proves that our algorithm can improve registration accuracy. Averagely, our algorithm can improve accuracy over un-corrected points by 20.45%.

If we look at the range from 40 to 70 degree, it fits the Equation 27 well. First as we just stated, all corrected points achieve better accuracy than un-corrected points. Second, all corrected points achieve similar accuracy. It means after using our algorithm to correct points, the registration accuracy is independent of intersecting angle between ultrasound image plane and object surface. While if we look at un-corrected points, the dependence is obvious. Smaller the intersecting angle is, larger the registration error will be. This is important for clinicians because in reality, catheter flexibility and the size of human heart chambers may prevent doctors from scanning with near 90 degree intersecting angles. Without our algorithm, any ultrasound image scanned with a smaller intersecting angle will deteriorate registration accuracy. Thus every scan must be done with great care. With our algorithm, registration can achieve better and consistent registration accuracy no matter how ultrasound image intersect with object surface. Thus clinicians can feel free to scan the heart shape in whatever way they feel convenient. This greatly reduces the work of clinicians while provide better registration accuracy.

4 4D Registration

The patient's heart is beating both during the CT scan and during the operation. The beating heart periodically changes its shape in a considerable magnitude. Such shape change can not be dealt with 3D registration. To capture all the shape change of the heart through a cardiac cycle, we scan a 4D heart model which is a series of 3D model across one cardiac cycle. All surface registration points will also have a time stamp stating when in a cardiac cycle it is captured.

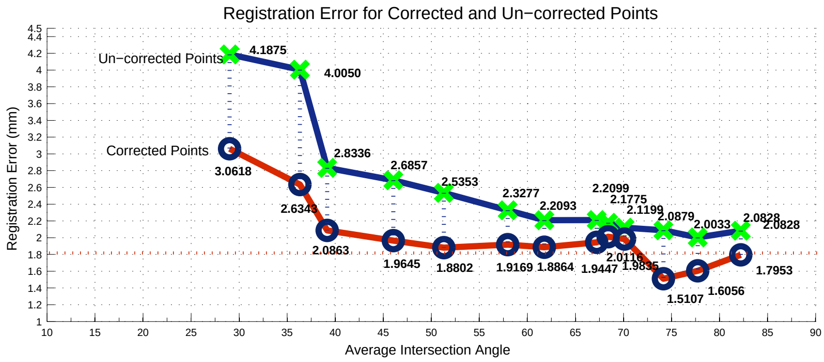

Figure 16: Registration accuracy and average intersecting angle between image planes and model's surface.

To register the 4D heart model with the magnetic position sensor, our system will automatically find a transformation function F that can align 4D surface registration points to the 4D heart model so that all the points are on the inner heart wall of the model. In our case, we also need to align the time axis. Next we will describe our method step by step in a time order.

4.1 4D Heart Model

CT scan is proceeded one day before the operation. We use GE's CT scanner which can generate a 3D heart scan at every 10% of a cardiac cycle, and totally 10 3D CT scans for one cardiac cycle. From the CT data, left atrium is segmented out manually. Then we extract the surface model from the segmented CT data using Marching Cube(MC) algorithm. The density threshold of MC algorithm is set to represent the surface between blood and heart muscle. The extracted surface should represent the inner heart wall. We remove the small floating parts by discarding all triangles except those in the largest connecting group of the model. Then we smooth the model based on geometry cues with an implicit integration method [8].

Each 3D surface model extracted from CT data corresponds to a time $t \in [0, 1)$ (suppose $t = 0$ is at the beginning of a cardiac cycle and $t = 1$ is at the end of a cardiac cycle) in a cardiac cycle when the CT was scanned. In the rest of the paper, we use $C = \{C_0, C_1, ..., C_{n-1}\}$ to represent the 4D heart model, n is the number of 3D models for one cardiac cycle. In our example we capture a 3D CT scan at every 10% of a cardiac cycle, we can extract $n = 10$ surface models $C = \{C_0, C_1, ..., C_9\}$ where each model C_i represents the heart shape at time $t = i/10, i = 0, 1, ...9$. This process is shown in Figure 17.

4.2 4D Surface Registration Points

At the beginning of the operation, the clinician needs to capture some points spread on the inner heart wall with magnetic position sensor (Figure 18(b)). During this step,

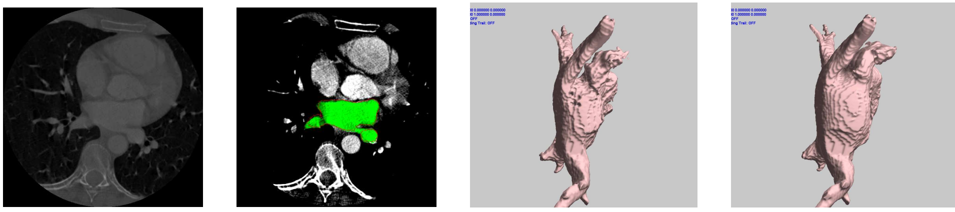

(a)CT scan (b)Segmented CT (c)Model t = 0.0 (d)Model t = 0.5

Figure 17: CT scan and 4D Heart Model of a patient. It contains 10 3D models for one cardiac cycle.

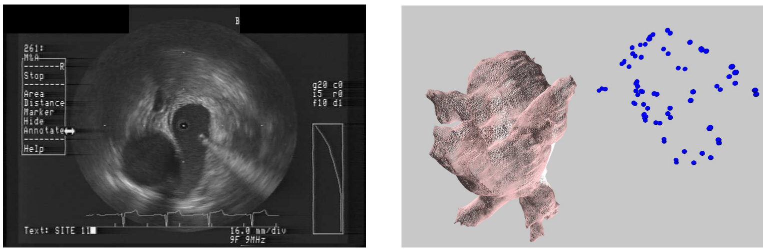

(a) Ultrasound Image (b) Captured Point Set

Figure 18: Constraint Point Set. (a) Ultrasound image with the ablation catheter tip visible in it. Clinicians can verify if the ablation catheter tip is touching the heart wall. (b) A set of captured points (blue dots) at $t = 0.0$. They are not aligned with the heart model yet.

usually another catheter with intracardiac echocardiography sensor, which can generate 2D ultrasound images as shown in Figure 18(a) in real time, is used to verify the touching of ablation catheter tip on the inner heart wall. As we have stated in section 2, we can use the new combined catheter to do this job. The magnetic tracking system can be setup to capture points at 10 evenly distributed time spots within a cardiac cycle as the CT scan, so each captured point will have a time coordinate of $t = 0, 0.1, ..., 0.9$. We group those points with same time coordinates together (though they may be captured in different cardiac cycles). Then all the recorded points can be organized into 10 groups: $P = \{P_0, P_1, ..., P_9\}$. P can be thought as a 4D point set.

4.3 Registration Algorithm

4.3.1 Initial Registration

Space initial registration can be done in a coarse-to-fine scheme. First a rough alignment can be found based on the orientation of the patient on the bed. This rough alignment can be further refined by some points captured on some designated regions of the heart. These regions should be easy to locate solely from ultrasound images, such as the entrance region of pulmonary veins. Then we find an alignment so that

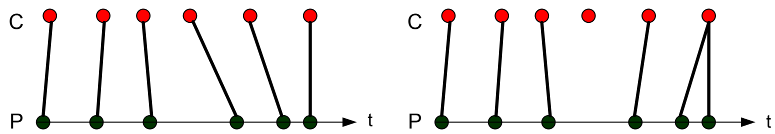

(a) Before time alignment (b) After time alignment

Figure 19: Time Alignment. Upper row represents models, lower row represents point sets. x axis represents time. (a) Initial time alignment, we assume it's simple one-on-one correspondence. (b) The best correspondence scheme will be found after time alignment.

these points are near the same regions in the heart model as where we know they are captured.

Time registration equals to a correspondence scheme S which tells for any point set P_i in P which C_j in C is its correspondence according to time. We know that we captured heart model $C = \{C_0, C_1, ..., C_9\}$ and points $P = \{P_0, P_1, ..., P_9\}$ both at $t = 0, 0.1, ..., 0.9$. Ideally the time registration should be P_i corresponds to C_i for any i. In reality, both the heart model and surface registration points are synchronized to ECG signal to determine the time coordinate. Under different conditions, sometimes the patient's heart beat rate is not stable, then this one-on-one correspondence of C_i with P_i may not be true. So time alignment is necessary (Figure 19). For initial time registration, we just use the correspondence scheme of P_i to C_i for any $i \in [0, 9]$.

Our 4D registration algorithm assumes errors have a gaussian distribution. Then it need to find a space transformation function F and a time correspondence scheme S that maximize the expectation of log likelihood of $p(F(P)|S, C)$. The probability $p(F(P)|S, C)$ can be defined as

$$p(F(P)|S, C) = \prod_i p(F(P_i)|C_{si}) = \prod_i (exp(-||F(P_i), C_{si}||)) \quad (28)$$

Here C_{si} is the corresponding model for P_i defined by scheme S. Each $p(F(P_i)|C_{si})$ can be defined as an exponential function of the average distance from every point in $F(P_i)$ to model C_{si}, which is written as $||F(P_i), C_{si}||$.

4.3.2 Space Registration

We can adjust the n (number of CT scanned within a cardiac cycle) and m (number of time spots the magnetic tracking system can record point coordinate) so that $n = m \times d$ where d is an integer. In ideal situation, we assume the t coordinates of magnetic tracked points and surface models from CT are perfectly synchronized. Then any magnetic tracked point in point set P_i should have the same t coordinate as heart model $C_{i \times d}$. Noted that if the t in CT and magnetic tracking system is not perfectly synchronized, this definite one-on-one correspondence may not exist. If we assume P_i is independent of all other C_j except the corresponding one $C_{i \times d}$,

$$p(F(P)|C) = p(F(P_1)|C_1) \cdot p(F(P_2)|C_{2 \times d})...p(F(P_m)|C_n) \quad (29)$$

where $n = m \times d$.

We define the probability of $p(F(P_i)|C_j)$ as the exponential function of the average square distance from each point in $F(P_i)$ to the surface model C_j:

$$p(F(P_i)|C_j) = exp(\frac{-\sum_{p_k \in P_i} ||p_k - C_j||^2}{|P_i|}) \tag{30}$$

we define the distance from a point to a model $||p_k - C_j||$ is the distance from point $p_k \in P_i$ to its nearest point in the surface model C_j. $|P_i|$ is the number of points in P_i.

To maximize the probability in equation (29), we can use a modified ICP[1] algorithm. ICP is widely used to iteratively minimize the distance between a set of points P and model C. In standard ICP algorithm, each iteration contains two steps:

- Compute the nearest point in Model C for each point in point set P.
- Find a transformation F that can minimize the distance from P to their nearest points. Then replace P with $F(P)$ and repeat.

In our case, during the first step, for each point set P_i, we find the nearest point set P_{near_i} only from model $C_{i \times d}$. In order to maximize the whole $p(F(P)|C)$ other than any single term of $p(F(P_i)|C_j)$, in the second step, we combine all the point sets together as well as their nearest point sets: $P_{combine} = \cup_{i=1}^{m} P_i$, $P_{near\_combine} = \cup_{i=1}^{m} P_{near\_i}$, and find a transformation F like in standard ICP for this combined point set $P_{combine}$ and $P_{combine\_near}$. In this way, we can find F that maximizes the probability $p(F(P)|C)$. The modified ICP can be summarized as:

- Compute the nearest point set P_{near_i} for each P_i in their corresponding model $C_{i \times d}$.
- Combine point sets: $P_{combine} = \cup_{i=1}^{m} P_i$, $P_{near\_combine} = \cup_{i=1}^{m} P_{near\_i}$, and find a transformation F that minimize the distance from $F(P_{combine})$ to $P_{near\_combine}$. Then replace the original P_i with $F(P_i)$ and repeat.

There are many ways to accelerate ICP and make it more robust. All those algorithms can be applied in our case. We use K-D tree acceleration for nearest neighbor search, and add random perturbation to found results and re-run ICP to ensure the convergence to global minimum.

4.3.3 Space-Time Registration

During the heart operation, the t coordinates from magnetic tracking system may not be perfectly aligned with those from CT data because they are captured during different days. This means point set P_i may not truly correspond to model $C_{i \times d}$. Then we need to find out the *time correspondence* as well as the *space alignment*.

We assume for any point set P_i, the possible corresponding model are $C_{i \times d}$ and its close neighboring models such as $C_{i \times d \pm k}$, for example if we take 4 neighbors then $k = [1, 2]$. This assumption is valid since we know the timing difference of magnetic tracked points and CT models are not very large. We write all the candidate models for a point set P_i as: C_{ij} where $j = [1, 5]$ if we use 4 neighbors and $C_{i \times d}$ itself. We define S a scheme that selects one C_{ij} as the corresponding model for each point set P_i.

The probability we need to maximize here becomes

$$p(F(P)|S, C)$$

which is very difficult to compute directly since we do not know S. Here we propose an EM algorithm that can maximize this probability by maximizing the expected log likelihood $log(p(F(P)|S, C))$, assuming S is a hidden random variable.

To use EM algorithm, we first need to figure out the Q function, or the expected log likelihood. If we think S is a random variable, then the expected log likelihood becomes:

$$Q(F(P), S, C) = \sum_S log(p(F(P)|S, C))f(S|C, F^{(k-1)}(P)). \tag{31}$$

$log(p(F(P)|S, C))$ is the log likelihood. $f(S|C, F^{(k-1)}(P))$ is the probability of a correspondence scheme S given the data C and alignment $F^{(k-1)}(P)$ found in last iteration. It can be computed by:

$$f(S|C, F^{(k-1)}(P)) = \frac{p(F^{(k-1)}(P)|C, S)p(S|C)}{\sum_S p(F^{(k-1)}(P)|C, S)p(S|C)} \tag{32}$$

where $p(F^{(k-1)}(P)|C, S)$ is the probability of transformed points in last iteration given model C, and the corresponding model for each point set P_i is determined by S. $p(S|C)$ is the prior probability of every correspondence scheme S.

Next we will show how to maximize this Q function.

In the E step We compute the probability $f(S|C, F^{(k-1)}(P))$ for any S with the following formula:

$$f(S|C, F^{(k-1)}(P)) = \frac{1}{a}p(F^{(k-1)}(P)|C, S)p(S|C) \tag{33}$$

Where a is the normalize term. Probability $p(F^{(k-1)}(P)|C, S)$ is computed with formula $\prod_{i=1}^{m} p(F^{(k-1)}(P_i)|C_{ij})$ where the corresponding C_{ij} for P_i is defined by S. $F^{(k-1)}$ is known, given correspondence from S, $p(F^{(k-1)}(P_i)|C_{ij})$ can be computed with equation (30). Now each $f(S|C, F^{(k-1)}(P))$ is known and we represent it by $f(S)$ in next step.

In the M step As we have the $f(S)$ which is the probability of any S given C and $F^{(k-1)}$, the Q function in equation (31) becomes

$$Q = \sum_S log(p(F(P)|C, S))f(S)$$

then to maximize the Q function is equivalent to maximize the function below:

$$\arg\max_F \sum_S logp(F(P)|C, S)f(S)$$

$$= \arg\max_F \sum_S log(\sum_{i=1}^{m} p(F(P_i)|C_{ij})_S) f(S)$$

$$= \arg\max_F \sum_S (\sum_{i=1}^{m} log(p(F(P_i)|C_{ij})_S)) f(S)$$

$$= \arg\min_F \sum_S (\sum_{i=1}^{m} ||F(P_i) - C_{ij}||_S) f(S)$$

Where the corresponding model C_{ij} is defined by S. Here we can see, the problem becomes to find a F to minimize a weighted distance function. For each scheme S, the distance function $||F(P_i) - C_{ij}||_S$ (in which the C_{ij} is the corresponding model of P_i defined by the particular S) is weighted by $f(S)$ computed in **E** step. This minimization can be done by our modified ICP algorithm described above. The only difference is here we add a weight when we combine the points together.

Then we replace the $F^{(k-1)}$ with the new F and repeat.

The EM algorithm stops when F doesn't change more than a certain threshold or the alignment error is below a certain threshold.

Initial Values of F is computed under the correspondence scheme in ideal situation where P_i corresponds to $C_{i \times d}$.

4.4 Experiment Result

4.4.1 3D Phantom Model Test

To validate our system, we tested it with a real patient's data. The CT scan's resolution is $512 \times 512 \times 116 \times 10$ (X×Y×Z×time). Voxel size is X: 0.48mm per voxel, Y: 0.48mm per voxel, Z: 0.625mm (or 1.25mm) per voxel, time: 10% of a cardiac cycle(Figure 17). Then we used a fast prototyping 3D printer to build a 3D heart phantom model based on the patient's CT scan model. Then we a used CARTO system by Biosense to track the catheter position (1mm average error) and inserted the catheter into the phantom model. An outside wave generater was used to simulate ECG/EKG signals and CARTO can capture position at the beginning of each cardia cycle. So here the points we have is $P = P_0$(Figure 18(b)). We collected 76 constraint points to do the registration: for every location, we recorded two points. Then the clinician proceeded the ablation procedure *without* our system's help and recorded all the ablation sites. Our system then mapped where those ablation sites are based on registration. The correctness of registration is verified by the clinician who knows where those ablation sites should be mapped to. The registration error is: 1.6347mm. Results are shown in Figure 20.

4.4.2 4D Synthetic Data Test

We tested our 4D registration with our synthetic data based on real patient's CT scan. First we loaded in the 4D CT scan model. Then we simulated a catheter with position sensor at tip moving into the heart. To fully exploit the information of a 4D heart model, we recorded surface points in such a way: we moved the simulated catheter to

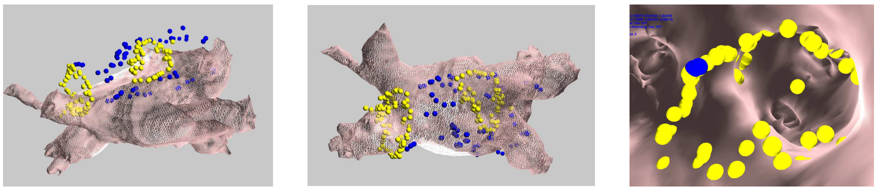

(a) (b) (c)

Figure 20: Patient data test (a) Initial alignment (intensionally deteriorated to test robustness). (b) Outside view of the registration result. Yellow points are ablation sites. They are correctly mapped to the pulmonary veins entrance regions. (c) Inside view, these points are right on the surface.

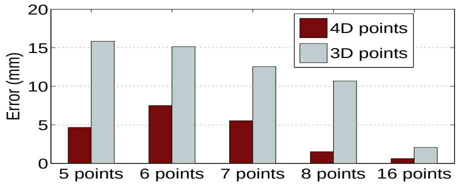

Figure 21: Constraint point number vs registration error. For each item, we run the registration test for several times and the average error is shown here. We can see with 4D points, less constraint points can achieve similar registration accuracy as 3D points.

touch the heart wall, stay on the wall for a cardiac cycle, and record all 10 positions $p = \{p_0, ..., p_9\}$ at time $t = 0, 0.1, ..., 0.9$, generally $p_i \neq p_j$ if $i \neq j$ because the heart is beating. For each location data, we added random noise of 1mm to simulate the position sensor error in reality. We can call p a 4D point. After we record one 4D point, we actually add one 3D point to each point set P_i, $i = 1$ to 10. No extra efforts are necessary to capture one 4D point than a 3D point. And we used a random transformation F_r to transform the points away from the heart model. F_r has $0 - 30$ degree of rotation and $0 - 20$mm of translation. Then we used our algorithm to find registration transformation F which maps points back to the surface model. We define the error as the average of $||v - F(F_r(v))||$ for every vertex v of the heart model. The result is shown in Figure 21. We also added 3D registration result for comparison. As we can see, 4D point registration achieves same registration accuracy with fewer constraint points than 3D point registration in our test. The spacial distribution of constraint point set is random but same for 3D and 4D points. Registration error also depends on F_r.

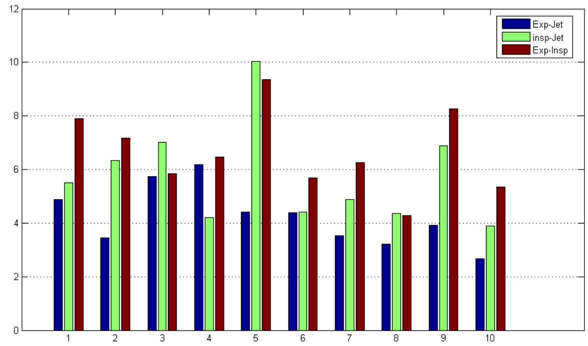

Figure 22: We recorded the 3D positions of ten locations on the left atrium during 3 breath phases: JET ventilation, End of expiration and Inspiration. And then measure the distances of these locations among the different breath phases. We found that the distance of JET to End-expiration is universally smaller than JET to Inspiration which means the heart shape during JET is closer to the heart shape during End-Inspiration than to the shape during Inspiration.

5 Local Non-rigid Registration

5.1 Medical Significance of Non-rigid Heart Shape Change

The left atrium is a highly motile and non-rigid object. Non-rigid shape changes result from multiple sources:

1. Cardiac cycle, or heart beat.
2. Breath cycle, the pressure change of the lung.
3. Others, like blood pressure, medicine and medical instruments.

Some shape change sources can be modeled or carefully removed. For the cardiac cycle, this shape change can be modeled and solved by our 4D registration using full-motion 4D heart model.

For breath, it changes the pressure of the lung and eventually change the shape of left atrium because they are adjacent to each other. We can use a high frequency ventilation machine which can maintain a constant pressure in lung to remove such shape changes during the operation. But the CT scan is usually done at the end of expiration or full inspiration. Our experiment data indicate that the heart shape at end-expiration is closer to the shape at JET ventilation (Figure 22). In this case, we scan CT at end-expiration. The heart shape at JET is still different from the heart shape at end-expiration. And such shape difference is non-homogeneous which means it can not be registered by any global rigid registration algorithm.

To demonstrate such local non-rigid heart shape difference we did the following experiment. We record the coordinate of 10 locations in left atrium during 3 breathing

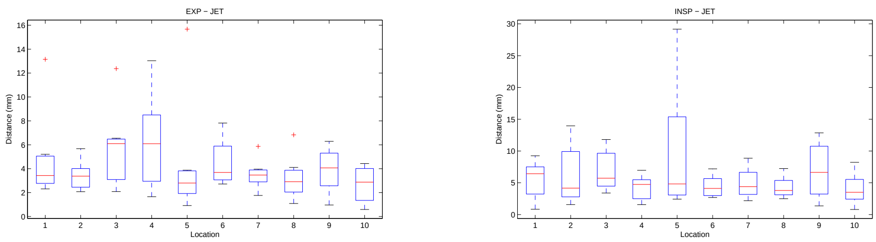

(a) (b)

Figure 23: Local non-rigid shape difference among breathing phases at 10 locations in left atrium. (a) EXP-JET difference. (b) INSP-JET difference.

phase: full inspiration (INSP), full expiration (EXP) and high frequency jet ventilation mode (JET). Then we use rigid global registration algorithm to register the points captured during the 3 breathing phases to eliminate any global shape differences. The rest is local non-rigid shape difference. We did this to 7 patients and result is shown in Figure (23). (a) is the EXP-JET difference. We can see on all 10 locations, there are around 4mm non-rigid shape differences. For INSP-JET in (b), the difference is around 5mm. If we do not consider such non-rigid property in our registration, we may have very unreliable results.

Other sources such as different blood pressure and medicines and instruments used during operation may also contributes slight non-rigid local shape change of the left atrium. Such heart shape changes can not be easily modeled.

In this case, we employ a free-form non-rigid registration which will be used after the 4D registration to further improve the registration accuracy.

5.2 Non-rigid Registration in Medical Image

In medical image society, rigid global registration algorithms have been well established and successfully used by many applications. But for operations on brain, liver, breast and heart, non-rigid registration is necessary. Many researchers have proposed many different non-rigid registration algorithms, which can be organized into several main catalogs [7]:

1. Affine and polynomial transformation
2. Optical flow based transformation
3. Physical based transformation
4. Smooth basis function

Affine and polynomial transformation is a natural extension of the traditional rigid object registration which only considers translation and rotation. Affine transformation adds shearing and scaling to the registration to adopt some non-rigid properties [27][5]. Basically this is still a global registration method because the non-rigid transformation will apply to the whole object.

Optical flow was designed to estimate motion between two consecutive image frames [14]. [13][12] use optical flow to register medical volumetric images. The similarity measurement of optical flow methods is based on image pixel intensities and then continuity constraint is applied to smooth the motion field. It can be a local transformation but with our application, points and surfaces, it is not intuitive to use optical flow. Also we already have correspondences between points and surfaces, we do not need image intensities to estimate such correspondence.

Physical based methods assume the images are elastic objects and apply forces to the object to non-rigidly deform the images for registration [10][6]. In [4] the method is based on viscous-fluid transformations. All these physical models are computationally expensive and a lot of parameters need to be fine-tuned to generate a good result. It is not suitable for our in-operation registration requirement.

[15] [20] [21] [19] use radial basis function as an interpolant to extend the non-rigid transformation function defined in some landmark points to the whole 3D space. Besides global thin-plate functions, compactly supported radial basis functions are also used to reduce the computation cost and maintain local properties. This compactly supported radial basis function registration method fits the requirement of our case: we know the non-rigid transformation function at some landmark points (surface registration points) and each landmark point should only affect the transformation locally. Next we will show the details of how we use radial basis function to do local non-rigid registration.

5.3 Non-rigid Registration Using Radial Basis Functions

Local non-rigid registration is to be applied after the 4D registration to further improve the registration accuracy. Suppose the intra-operative surface registration point set is $P = (p_1, p_2, ..., p_n)$, and the heart model from CT is C. After global rigid registration, P and C still have difference $D = (d_1, d_2, ..., d_n)$. Here P is after the global registration. Each d_i is defined as:

$$d_i = p_i - C_{p_i}$$

Where C_{p_i} is the nearest point of p_i in model C. The free-form non-rigid registration should find a transformation function $F_{local}(C)$ so that for any $i \in \{1, 2, ..., n\}$,

$$p_i = F_{local}(C_{p_i}) \tag{34}$$

which means after this non-rigid local transformation F_{local}, all the surface registration points should be on surface the transformed model $F_{local}(C)$. Usually the $F_{local}(p)$ at any 3D position $p = (x, y, z)$ has the form of:

$$F_{local}(p) = p + \sum_{i=1}^{n} a_i \cdot \Phi(||p - C_{p_i}||) \tag{35}$$

$|| * ||$ is the distance between two 3D points. a_i is a 3D vector, also known as the coefficient for each point C_{p_i}. $\Phi()$ is a radial basis function. For any point p, $F_{local}(p)$ is to add an offset to p. The offset is a weighted sum of all coefficients a_i

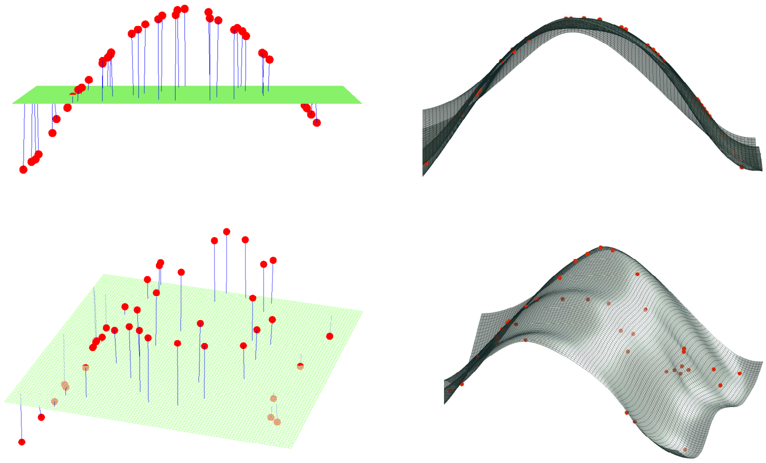

(A) (B)

Figure 24: An example of non-rigid local registration. (A) shows the model (green plane) can not be better aligned to the surface points (red balls) with rigid global registration. (B) shows after our non-rigid local registration, the surface can be corrected according to the surface points.

weighted by the radial basis function of the distance from p to C_{p_i}. $||p - C_{p_i}||$ can be easily computed. a_i is unknown now. With the constraint in equation (34) we can have enough equations to solve each a_i:

$$p_i = C_{p_i} + \sum_{k=1}^{n} a_k \cdot \Phi(||C_{p_i} - C_{p_k}||) \tag{36}$$

We choose one of Wu's [28] compactly supported positive definite radial basis function which can ensure there is solution for equation (36):

$$\Phi(X) = \phi(\frac{||X||}{s}) \tag{37}$$

$$\phi(r) = (1-r)_+^4(3r^3 + 12r^2 + 16r + 4), r \geq 0 \tag{38}$$

where $(1-r)_+ = max(1-r, 0)$, s is a pre-defined scale to determine each C_{p_i} can affect points how far away. This compactly supported radial basis ensure that each surface registration points only affect the non-rigid transformation locally. Also it can reduce the computational cost. Moreover (38) has been shown to have C^2 continuity. Therefore, the F_{local} is C^2 continuous in the space and it satisfied the constraint shown in (34).

One example of this non-rigid local registration is shown in Figure 24. Suppose we have a 3D model of a plane, and we have several surface points that shows the object is actually is curved. Rigid global registration can not find a good alignment of the points

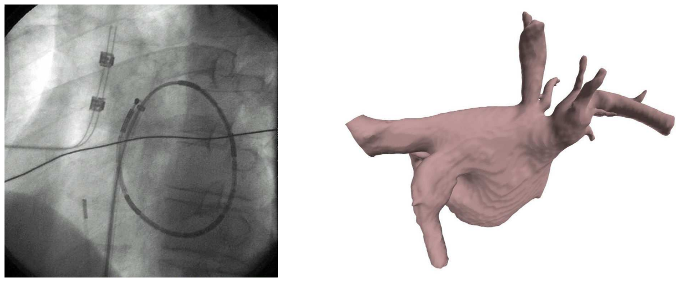

(a) (b)

Figure 25: Visualization: (a) usually what doctors will see with only fluoroscopy. (b) our system can provide much better visualization.

and the model (Figure 24 (A)). Using our radial basis local non-rigid registration, we can modify the model according to the surface points locally and non-rigidly. The result is a much better fit for the points (Figure 24 (B)).

6 Visualization for Navigation

After registration, we need to display the heart model and positions of different medical instruments such as ablation catheter in the same monitor. This visualization actually helps doctors to navigate inside the patient's heart.

With registration and position sensors tracking the catheter tips, we can provide many ways to visualize the surgery region: we can render the global view as if doctors can see through skins and muscles and clearly see where their catheters are inside the heart. This is like a fluoroscopy image just without radiation (Figure 25). Or we can put a virtual camera at the tip of the catheter so that doctors feel they are sitting at the catheter tip and they can "fly" the catheter to where they want to go. This is like a fiber-optic camera fit to the catheter just without the interference from the darkness and blood inside heart (Figure 26).

Also doctors can easily make labels on the heart model surface or map data to it. We can easily load some pre-operative planning data and guide doctors to finish the surgery. With surface model and position sensor, we can visualize the surgery as any other system can and enhance it for a better view (Figure 27).

Clipping planes and other graphics techniques can generate views that is impossible to get in real world and unveil more details of the patient's heart to doctors to make better decision (Figure 28).

7 Conclusion

In this thesis, an image guided navigation system for minimally invasive surgery is presented. The core of this system is a 3D ultrasound catheter which can scan a patient's heart with ultrasound image plane during the operation. Because it does not require

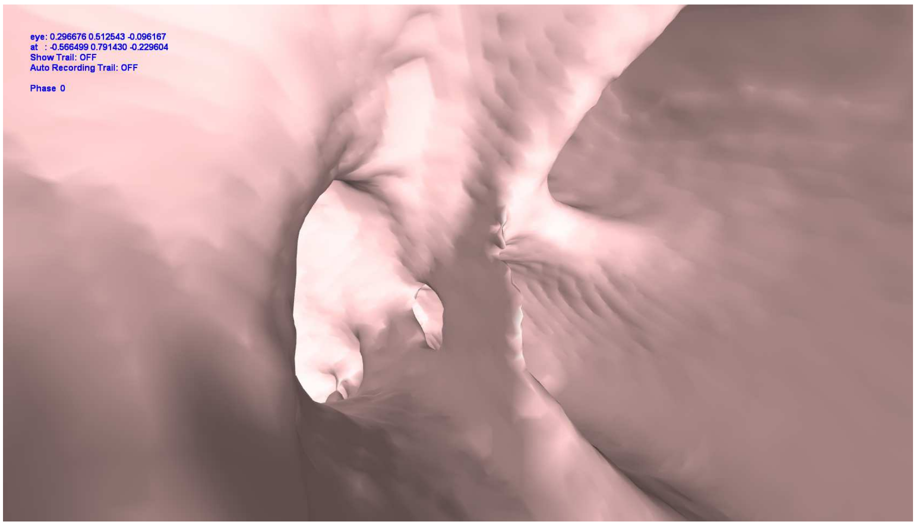

(a)

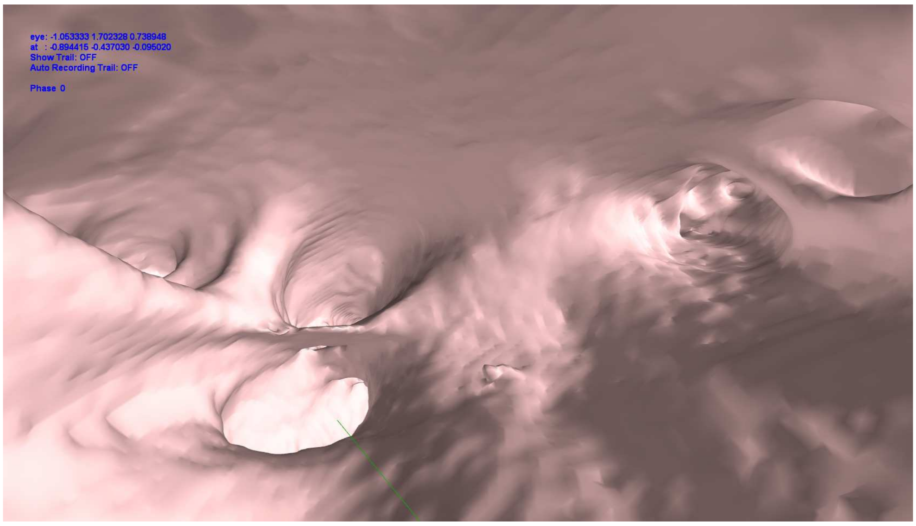

(b)

Figure 26: Visualization: (a) we can put a virtual camera at the tip of a catheter and doctors then can ”fly” the catheter to where they want to. It can give much better visualization and much more freedom than to actually put a fiber-optic camera at the catheter because there is no illumination problem and there is no blood to block our sight. (b) super-wide angle of view put both left and right pulmonary veins into the same picture. It helps doctors to have better global view of the left atrium without pulling the virtual camera outside the atrium.

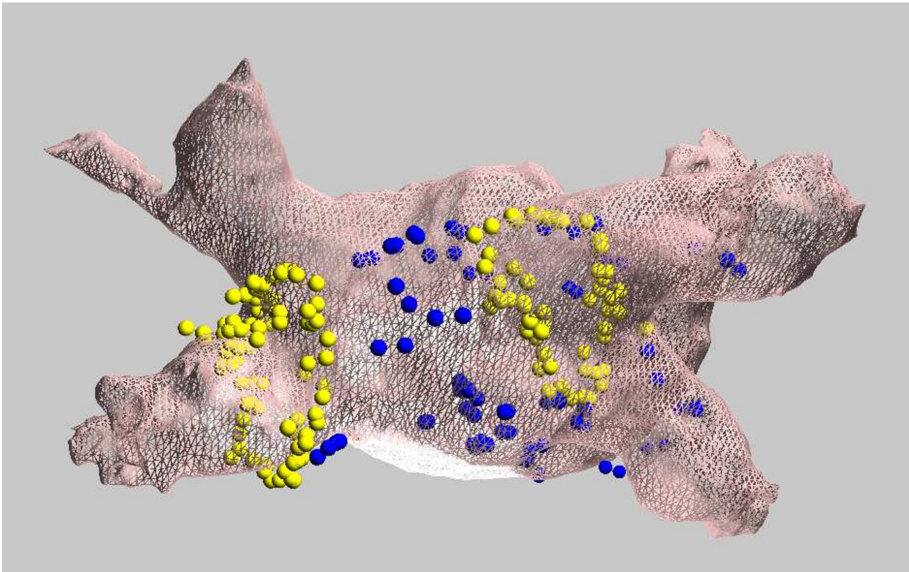

(a)

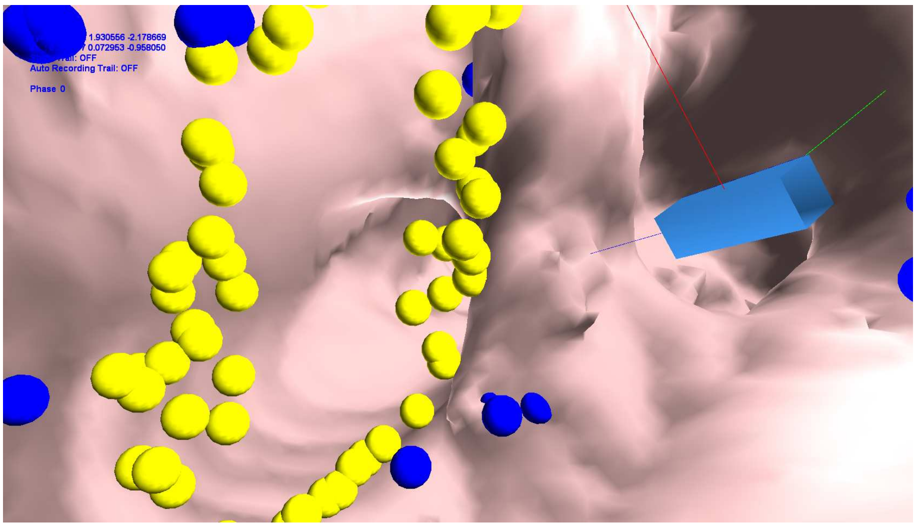

(b)

Figure 27: Visualization: Data mapping. We can map different data onto the surface model such as pre-operative planning data and ablation locations. With data mapping, doctors can get more information than direct visualization of the heart.

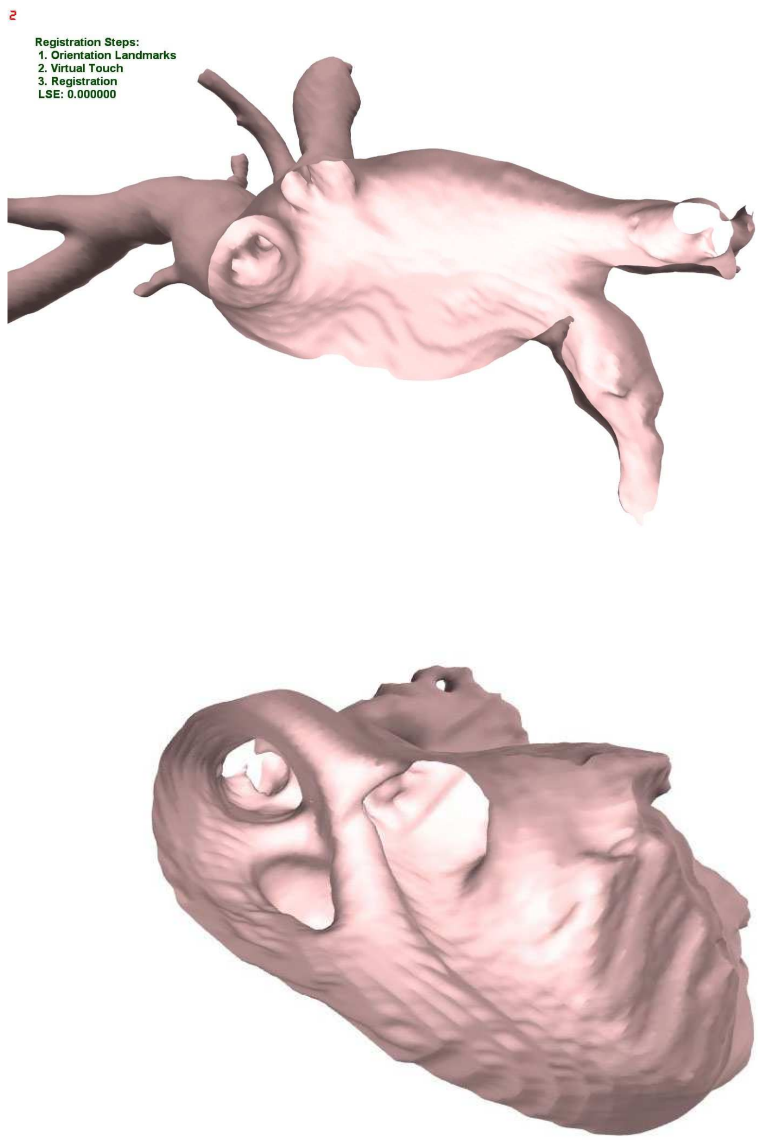

Figure 28: Visualization: with clipping plane we can unveil more details of the patient's heart than doctors can see in real world. Pictures show we virtually cut the left atrium in half and display the detailed inside view of it.

physical touch on the heart wall, we call it “virtual touch”. This scanning procedure is hundreds of times faster than current method of manually collecting shape information. Then it can automatically reconstruct the 3D or 4D shape of the heart it scanned. Our system have the ability to correct 3D reconstruction error caused by finite ultrasound image plane thickness. With this intra-operative shape measurement, we can register it with high-resolution pre-operative heart images such as CT or MRI images. After registration, high-resolution pre-operative heart models can be displayed with magnetically tracked catheters in one monitor so that doctors can intuitively navigate catheters to desired locations.

Because patient’s hearts are beating during operation, we extended our system to 4D (time+space). To deal with cardiac cycles, we use 4D heart model and synchronize all our “virtual touch” model points to ECG/EKG signals. To reduce the effect of breathing cycle, we use a high frequency ventilation machine to keep the pressure of lung in a constant state. The registration algorithm then involves space registration as well as time registration. An EM algorithm is presented to do both time and space registration iteratively.

Since heart is not a rigid object, the shape of the heart may have slight changes from day to day under different conditions. This non-homogeneous shape change cannot be captured by any rigid object registration algorithms. We included a local non-rigid registration after global rigid registration to deal with this problem.

With all the features we’ve provided, our navigation system can achieve faster speed, better accuracy and more intuitive navigation experience than current available system.

Parts of the thesis have been published in [29], [30] and [31].

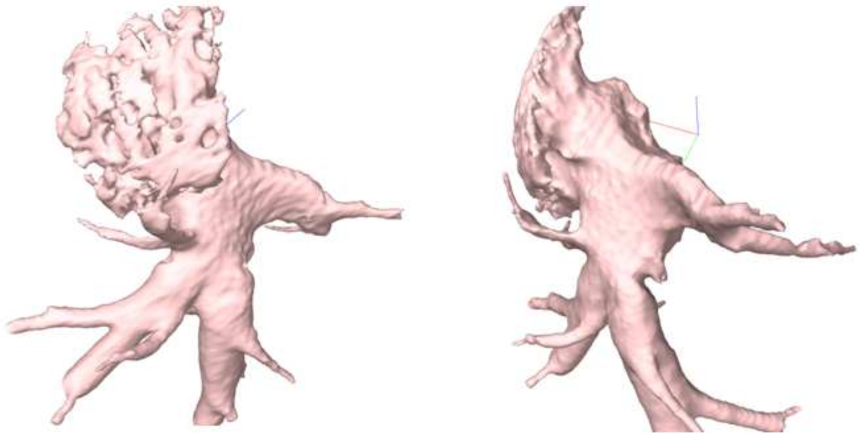

Figure 29: The surface model of the pig's left atrium

APPENDIX

A Animal Test

We have conducted one animal test with the prototype of our system. The result is mixed. We discovered some practical problems when apply the whole system into real clinical situations.

A.1 Test Setup

The test subject is a pig. We did CT scan of the pig's heart 1 week before the test. We segmented out left ventricle and left atrium of the pig's heart. During the test, we only scanned and registered the left atrium. The 3D surface model of the left atrium is shown in Figure 29.

A.2 Test Result

Both during the CT scan and operation, the pig is under deep sedation and breath with a high frequency ventilation machine. During the test, our virtual touch catheter inserted into the left atrium and the doctor tried to scan the chamber with ultrasound image plane. During the scan, a total of 7786 surface points have been captured and then registered to the surface model of the left atrium. The registration result is shown in Figure 30. The average distance from virtual touch surface points to surface model is 3.95mm.

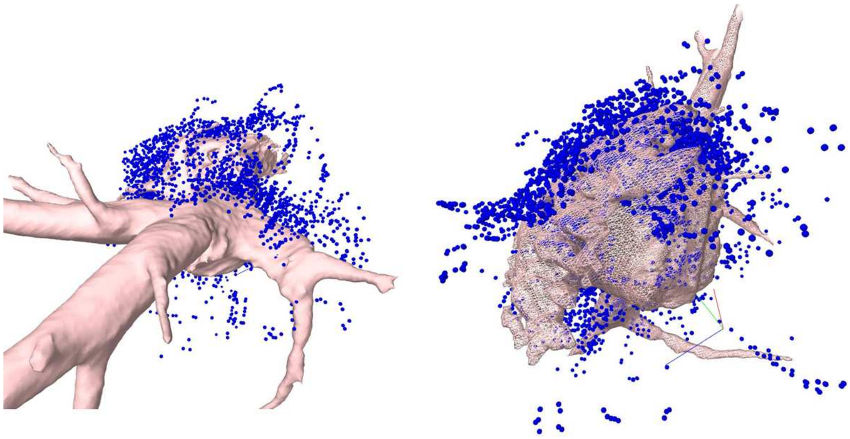

Figure 30: Registration of the virtual touch points with surface model. Average error is: 3.95mm.

A.3 Result Analysis

From the animal test, we discovered quite a few ways to improve our system. Also we found something that we need to avoid to minimize registration errors.

A.3.1 Surface Point Density

With each ultrasound image, our system can capture tens or hundreds of surface points. During the test, some parts of the left atrium have been repeatedly scanned and other areas, because of difficulties to access, has hardly been scanned. Thus the distribution of our virtual touch points is not uniform. From Figure 31 we can see some parts have dense points while some parts have scarce points. This bias on point density will eventually affect final registration: the final registration will try to accommodate the densely scanned areas while ignore less densely scanned areas.

To deal with such density bias, we added a density control component to our virtual touch system. Before the scan, doctors can setup a maximum density value which means the maximum number of surface points our system can accept in a certain volume. For example, 1 points for every cubic millimeter. Then the density control unit will dynamically monitor each newly scanned point to see if adding this point will exceed the density limit. If not, the point will be added to the intra-operative model just as before. If it does exceed the density limit, the density control unit will randomly drop one point in the voxel to maintain the acceptable density. Also the which point to drop can be done with some sophisticated rules based on the quality or confidence of the points. Such density control can reduce some bias but not all. Because some part of left atrium may have zero point scanned. And even by limit the density in easy-to-scan areas, it is still biased.

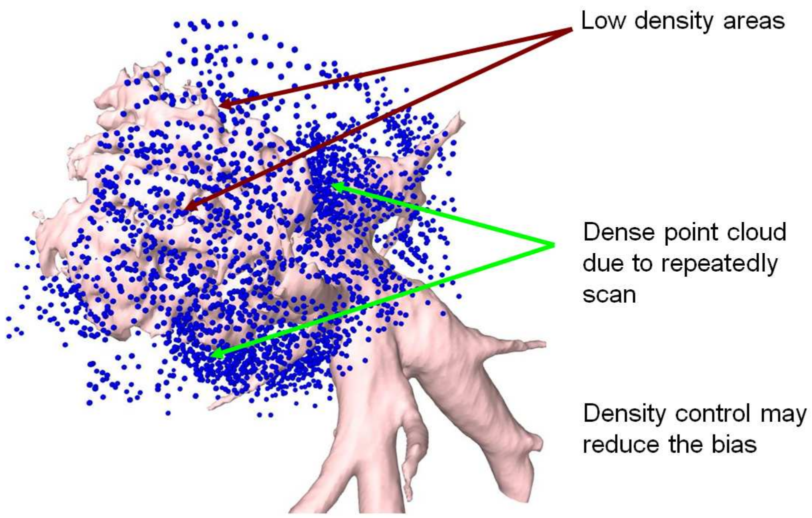

Figure 31: Density of surface registration points

A.3.2 Valve

As seen in our segmented left atrium model, the whole chamber is closed. But in reality, there is a valve connecting this left atrium with left ventricle. And this valve opens at 0% of the cardiac cycle to which all our CT scan and virtual touch can synchronized.

As shown in Figure 32 (a), left: the segmented model we had is a closed model while in reality, it should be like the right one. During the virtual touch scan, because the valve is open at 0% of the cardiac cycle, with our wall pixel detection algorithm, some surface from left ventricle then is included.

To solve this problem, we can first modify the CT scan model to make the valve open. And for virtual touch scan, we can add some dynamic outlier control unit to eliminate points that are too far away from the main point cloud. Usually such points are from left ventricle. But this method won't eliminate every point from other chamber when valve is open because with an open valve the two chamber actually become one. Possible solution could be: 1) include left ventricle surface model in registration 2) Synchronize all the scan to some other time of a cardiac cycle when the valve is closed.

A.3.3 Complex Geometry

For pig's left atrium, the appendage is relatively larger than human's. As shown in Figure 33, the shape of appendage has very complex geometry. Such a shape introduces great difficulties for both CT scan and virtual touch scan to reliably reconstruct the 3D surface. Unfortunately, during our test, majority of virtual touch scan points are from the appendage. Such points greatly reduced the accuracy of our registration.

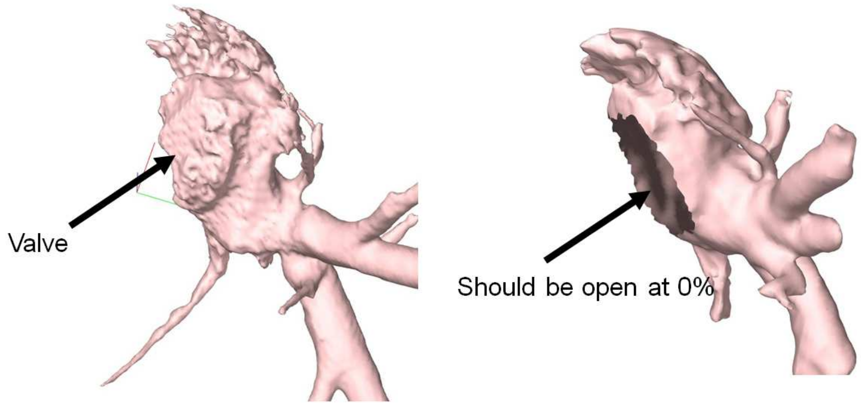

(a) Valve should be open

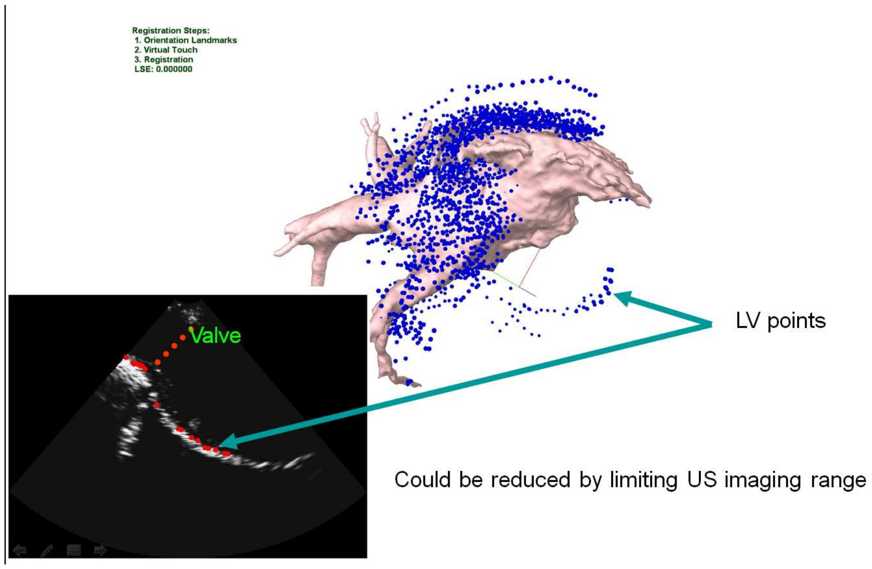

(b) Valve leak

Figure 32: Valve on left atrium introduce errors both for CT scan and virtual touch scan

A.3.4 Limited Accessibility

Because of the size of the pig's left atrium and catheter, and the limited flexibility of the catheter, our virtual touch can only scan certain areas of the left atrium while left large areas inaccessible. As shown in Figure 34, the visible area for our virtual touch catheter are focused at valve (which opens during 0% of the cardiac cycle and reveal the left ventricle chamber) and appendage (which has complex geometry). More stable parts are not visible to ultrasound virtual touch due to the insert location and orientation.

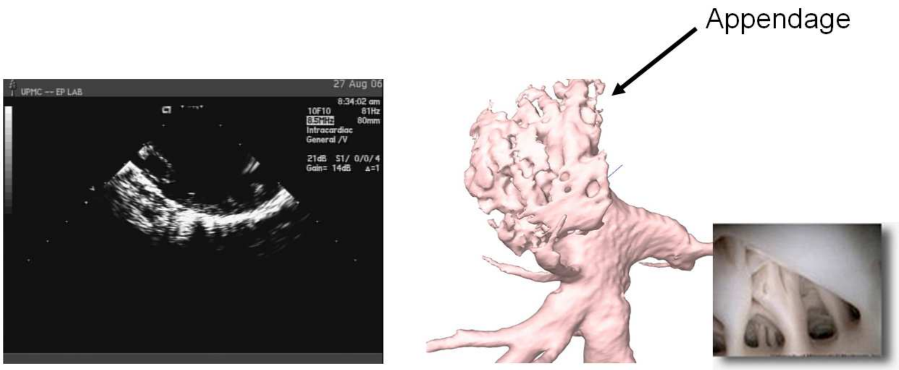

Figure 33: Complex geometry of the appendage affects registration accuracy

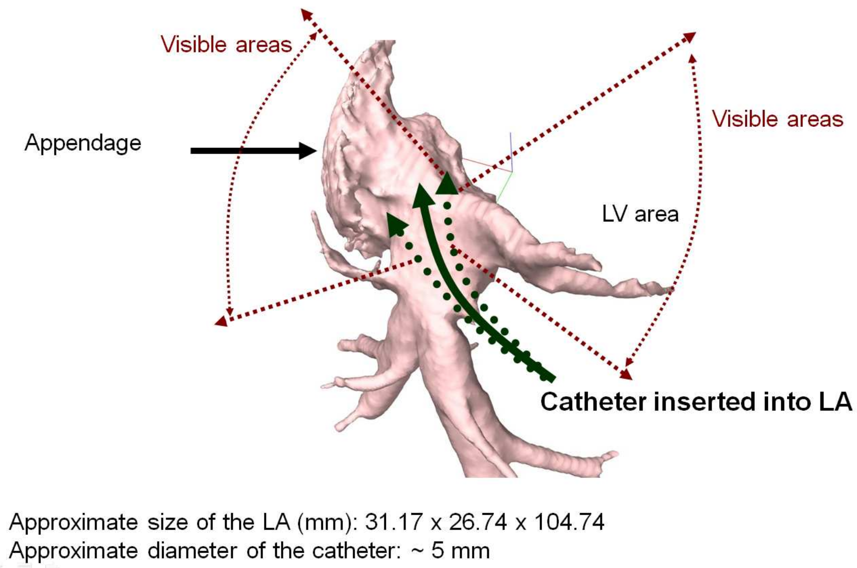

Figure 34: Not the whole left atrium can be scanned

Solution for this problem could be: 1) carefully planned insertion location and orientation. 2) test with some other chamber such as left ventricle which has much stable and simple geometry than left atrium.

A.4 Conclusion

The first animal test we did confirmed that our system can quickly build an intra-operative heart model and register it with pre-operative CT scan model to generate a combined shape measurement for navigation. With the result and analysis, we also discovered many practical problems. Most of them can be fixed with our proposed solution and some of them require further research. After all, the navigation problem is a hard problem and it needs more effort to put in before it can be fully deployed in surgical room.

References

[1] P. J. Besl and N. D. McKay. A method for registration of 3-d shapes. In *IEEE Trans. Pattern Analysis and Machine Intelligence*, pages 14:239–256, 1992.

[2] F. J. Canny. A computational approach to edge detection. In *IEEE Trans. Pattern Analysis and Machine Intelligence*, pages 13: 775–790.

[3] Dmitry Chetverikov and Dmitry Stepanov. Robust euclidean alignment of 3d point sets. In *First Hungarian Conference on Computer Graphics and Geometry*, pages 70–75, 2002.

[4] G. E. Christensen. Deformable tem-plates using large deformation kinemetics. *IEEE Transaction on Image Processing*, 5:1435–1447, 1996.

[5] D. L. Collins, P. Neelin, T. M. Peters, and A. C. Evans. Automatic 3d intersubject registration of mr volumetric data in standardized talairach space. *Journal of Computer Assited Tomography*, 18(2):192–205, 1994.

[6] Ch. Davatzikos. Spatial transformation and registration of brain images using elastically deformable models. *Computer Vision and Image Understanding*, 66(2):207–222, 1997.

[7] B. M. Dawant. Non-rigid registration of medical images: Purpose and methods, a short survey. In *Biomedical Imaging, 2002 Proceedings. IEEE International Symposium on*, pages 465–468, 2002.

[8] Mathieu Desbrun, Mark Meyer, Peter Schröder, and Alan H. Barr. Implicit fairing of irregular meshes using diffusion and curvature flow. *Computer Graphics*, 33(Annual Conference Series):317–324, 1999.

[9] Jun Dong, Hugh Calkins, Stephen B. Solomon, Shenghan Lai, Aarshan Dalal, Al Lardo, Erez Bren, Ronald D. Berger, Henry Halperin, and Timm Dickfeld. Integrated electroanatomic mapping with three-dimensional computed tomographic images for real-time guided ablatoins. *Circulation of Journal of the American Heart Association*, 113:186–194, 2006.

[10] J. C. Gee, M. Reivicj, and R. Bajcsy. Elastically deforming 3-d atlas to match anatomical brain images. *Journal of Computer Assisted Tomography*, 17(2):225–236, 1993.

[11] Di Gioia and etc. Hipnav: Pre-operative planning and intra-operative navigational guidance for acetabular implant placement in total hip replacement surgery. In *Computer Assisted Orthopaedic Surgery Symposium*, November 1995.

[12] P. Hellier and C. Barillot. Cooperation between local and global approaches to register brain images. In *Information Processing in Medical Imaging IPMI'01*, pages 315–328, 2001.

[13] P. Hellier, C. Barillot, E. Memin, and P. Perez. Hierarchical estimation of a dense deformation field for 3d robust registration. *IEEE Transactions on Medical Imaging*, 20(5):338–402, 2001.

[14] B. Horn and B. Schunck. Determining optical flow. *Artificial Intelligence*, 17:185–203, August 1981.

[15] C. R. Meyer, J. L. Boes, B. Kim, and et al. Demonstration of accuracy and clinical versatility of mutual information for automatic multimodality image fusion using affine and thin plate spline warped geometric deformations. *Mdeical Image Analysis*, 3:195–206, 1997.

[16] R. W. Prager, R. N. Rohling, A. H. Gee, and L. Berman. Rapid calibration for 3-d freehand ultrasound. In *Ultrasound in Medicine and Biology*, pages 24(6):855–869, 1998.

[17] Vivek Y. Reddy, Zachary J. Malchano, Godtfred Holmvang, Ehud J. Schmidt, Andre d'Avila, Christopher Houghtaling, Raymond C. Chan, and Jeremy N. Ruskin. Integration of cardiac magnetic resonance imaging with three-dimensional electroanatomic mapping to guide left ventricular catheter manipulation. *Journal of the American College of Cardiology*, 44(11):2202–13, 2004.

[18] Bruno Richard. Test object for measurement of section thickness at us. *Radiology*, 211:279–282, 1999.

[19] G. K. Rohr, A. Aldroubi, and B. M. Dawant. The adaptive bases algorithm for non-rigid registration. In *Proceedings of SPIE Medical Imaging 2002*, pages 933–944, 2002.

[20] G. K. Rohr, H. S. Stiehl, R. Sprengel, T. M. Buzug, J. Weese, and M. H. Kuhn. Landmark-based elastic registration using approximating thin-plate splines. *IEEE Transaction on Medical Imaging*, 20(6):526–534, 2001.

[21] D. Rueckert, L. I. Sonoda, C. Hayes, D. L. G. Hill, M. O. Leach, and D. J. Hawkes. Nonrigid registration using free-form deformations: application to breast mr images. *IEEE Transaction on Medical Imaging*, 18(8):712–721, 1999.

[22] David Schwartzman, Raveen Bazaz, and John Nosbisch. Catheter ablation to suppress atrial fibrillation: Evolution of technique at a single center. *Interventional Cardiac Electrophysiology*, 9:295–300, 2003.

[23] David A. Simon and Takeo Kanade. Geometric constraint analysis and synthesis: methods for improving shape-based registration accuracy. In *CVRMed*, pages 181–190, 1997.

[24] ML. Skolnick. Estimation of ultrasound beam width in the elevation (section thickness) plane. *Radiology*, 180:286–288, 1991.

[25] Atul Verma, Nassir F. Marrouche, and Andrea Natale. Novel method to integrate three-dimensional computed tomographic images of left atrium with real-time electroanatomic mapping. *Cardiovasc Electrophysiol*, 26:365–370, 2004.

[26] Atul Verma, Nassir F. Marrouche, and Andrea Natale. Pulmonary vein antrum isolation: Intracardiac echocardiography-guided technique. *Cardiovasc Electrophyisol*, 15:1335–1340, 2004.

[27] R. P. Woods, S. T. Grafton, J. D. Watson, N. L. Sicotte, and J. C. Mazz-iotta. Automated image registration: Ii. intersubject validation of linear and nonlinear models.

[28] Z. Wu. Multivariate compactly supported positive definite radial functions. In *AICM*, volume 4, pages 283–292, 1995.

[29] H. Zhong, T. Kanade, and D. Schwartzman. Sensor guided ablation procedure for left atrium endocardium. In *Proc. of MICCAI 2005*, pages LNCS 3750: 1–8, 2005.

[30] H. Zhong, T. Kanade, and D. Schwartzman. 'virtual touch': An efficient registration method for catheter navigation in left atrium. In *Proc. of MICCAI 2006*, pages LNCS 4190: 437–444, 2006.

[31] H. Zhong, J.M. Lacomis, and D. Schwartzman. On the accuracy of cartomerge for guiding posterior left atrial ablation in man. *Heart Rhythm*, 4:595–602, 2007.